Z. Kristallogr. 219 (2004) 278–294

Structural variation and crystal chemistry of $LiMe^{3+}Si_2O_6$ clinopyroxenes Me^{3+} = Al, Ga, Cr, V, Fe, Sc and In

Günther J. Redhammer* and Georg Roth

Institute of Crystallography, Rheinisch-Westfälische Technische Hochschule (RWTH) Aachen, Jägerstraße 17/19, D-52056 Aachen, Germany

Received February 17, 2003; accepted February 11, 2004

Li–clinopyroxenes / Crystal chemistry / Single crystal structure analysis / X-ray diffraction

Abstract. A total of 32 synthetic end-member and solid-solution compounds of the $LiM^{3+}Si_2O_6$ (Li = M2 site, M^{3+} = M1 site = Al, Ga, V, Fe, Sc and In) clinopyroxene series have been investigated by single-crystal X-ray diffraction. Except $LiCrSi_2O_6$, all compounds show *C2/c* symmetry at 295 K. $LiCrSi_2O_6$ has space group $P2_1/c$ but transforms to the high temperature *C2/c* structure at 335 K. The variations of structural parameters in the $LiMe^{3+}Si_2O_6$ clinopyroxenes are dominated by the Me^{3+} site. The average M1–O bond length is linearly correlated with the ionic radius of the M1 cation. Octahedra reflect the increasing size of the M1 cations by steadily increasing bond and edge lengths, the variations however are not uniform. With increasing size of the M1 cation, octahedra deviate from ideal octahedral geometry. Octahedral edges, shared with other structural units, are distinctly hampered in expansion with increasing size of the M1 cation. The increasing size of the M1 octahedral chain is compensated by changing the kinking of the tetrahedral chain and by alterations of bond and edge lengths as well as the bond angles within the tetrahedron. Three different mechanisms of adapting of the structural building units with increasing M^{3+} cationic radius can be identified: (i) expansion of the tetrahedral chain by stretching (ii) transition form "O" to "S" chain conformation after full expansion and (iii) finally a limit of expansion in *a* direction. We stress that cations larger than In^{3+} cannot be substituted at the M1 site because of too large geometrical differences between octahedral and tetrahedral chains.

Introduction

The structure of the clinopyroxenes is very flexible and accepts a variety of cations, particularly on the octahedral M1 site. Hence, this mineral group appears to be well suited for a systematic study of structural changes over a wide range of compositions, most of which do not occur as minerals. For the Lithium-pyroxenes $LiM^{3+}Si_2O_6$ with Li = M2 site and M^{3+} = M1 site, only spodumene α-$LiAlSi_2O_6$ is found in nature, however, synthetic compounds with M^{3+} = Ga, Cr, Fe, V, Sc and In are known to exist.

Ito and Frondel (1968) were the first to synthesise the Sc^{3+} analog of spodumene, while the Li-pyroxenes with M^{3+} = V, Cr, and Fe first were described by Brown (1971) who used dry synthesis experiments near 1000 °C. Later Drysdale (1975) reported the hydrothermal synthesis of compounds with M^{3+} = Fe, Cr, V, Sc and In. Behruzi, Banerjea-Appel, Hahn and Scherberich (1984a) synthesised single crystals of $LiFeSi_2O_6$ and $LiCrSi_2O_6$ by using a high-temperature flux growth technique. A similar method was used by Grotepaß, Behruzi and Hahn (1983) to grow $LiScSi_2O_6$ and $LiInSi_2O_6$ single crystals. Very recently Redhammer, Roth, Paulus, André, Lottermoser, Amthauer, Treutmann, Koppelhuber-Bitschnau (2001) produced single crystals of $LiFeSi_2O_6$ by high-temperature/high-pressure synthesis at 1573 K and 2.5 GPa.

Lithium-pyroxenes are chain silicates and have monoclinic symmetry (freqeuntly *C2/c*) at room temperature. The structure consists of alternating chains of SiO_4 tetrahedra and ribbons of edge-sharing M1–O-octrahedra (containing the M^{3+} cation) linked via common edges to irregular M2-polyhedra with six-fold oxygen-coordination (containing the Li^+ cation). The chains and ribbons are running along the crystallographic *c*-axis. Figure 1 shows a representation of the crystal structure of $LiCrSi_2O_6$ as an example.

The structures of $LiAlSi_2O_6$ and $LiFeSi_2O_6$ were first investigated by Clark, Appleman and Papike (1969). Hawthorne and Grundy (1977) determined the structure of $LiScSi_2O_6$, and Behruzi, Hahn, Prewitt and Baldwin (1984b) found that $LiCrSi_2O_6$ crystallises in space group $P2_1/c$ at room temperature. Grotepaß et al. (1983) determined the crystal structure of $LiInSi_2O_6$. However, structural information given by Behruzi et al. (1984b) and Grotepaß et al. (1983) is very limited (e.g. no fractional atomic coordinates, bond lengths and angles). $LiGaSi_2O_6$ and $LiVSi_2O_6$ have been investigated by single-crystal methods by Sato, Osawa and Ohasi (1994) and by Satto, Millet and Galy (1997) respectively. Very recently Ohashi (2003) presented structural details on a large number of alkali-clinopyroxenes including the solid solution series

* Correspondence author (e-mail: guenther.redhammer@aon.at)

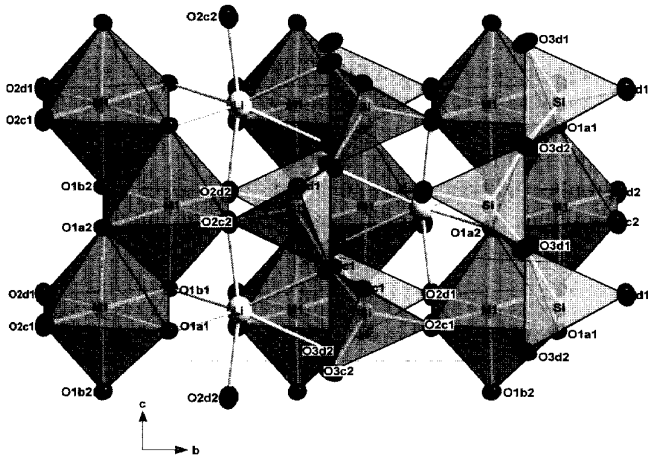

Fig. 1. Structure of $LiCrSi_2O_6$, viewed approximately along the *a*-axis. The labelling of atoms is chosen according Burnham, Clark, Papike and Prewitt (1967)

Li(Al, Ga)Si_2O_6 and Kopnin, Sato and Takayama-Muromachi (2003) gave first structural details on the compound $LiTiSi_2O_6$.

Besides all the published work, there is no detailed crystal chemical consideration of the complete Li-pyroxene series up to now. Thus in the present study, we have synthesised a series of end-member compositions $LiM^{3+}Si_2O_6$ with Me^{3+} = Al, Ga, Cr, Fe, V, Sc, and In as well as compounds on the $Li(Fe_{1-x}Sc_x)Si_2O_6$ and $Li(Sc_{1-x}In_x)Si_2O_6$ solid solution series and subsequently investigated these samples by single-crystal X-ray diffraction in order to (i) refine the structures of $LiCrSi_2O_6$ and $LiInSi_2O_6$ and (ii) to give a improved and refined crystal chemical description of $LiMe^{3+}Si_2O_6$ clinopyroxenes, not available so far in the literature. A study of the low temperature (80 K $\leq T \leq$ 296 K) structural properties of the samples investigated here is presented in a companion paper (Redhammer and Roth, 2004).

Sample material and experimental

Single crystals of $LiAlSi_2O_6$, $LiGaSi_2O_6$, $LiFeSi_2O_6$ and $LiScSi_2O_6$ were prepared from mixtures of Li_2CO_3, Al_2O_3, Ga_2O_3, Fe_2O_3 or Sc_2O_3 and SiO_2 in the stoichiometry of the desired composition (Table 1). The finely ground start-

Table 1. Details on single-crystal growth experiments.

Composition	run	*x*	method	*T* (K)	rate	*P* (GPa)	*t* (h)
$LiAlSi_2O_6$	LiAl	–	HP	1573	–	2.5	81
$LiGaSi_2O_6$	LiGa	–	HP	1573	–	2.5	78
$LiVSi_2O_6$	LiV	–	HP	973	–	0.4	237
$LiCrSi_2O_6$	LiCr	–	flux	1373 → 973	6 K/h	0.0001	103
$LiFeSi_2O_6$	LiHP	–	HP	1573	–	3.0	97
$Li(Fe_{1-x}Sc_x)Si_2O_6$ solid solution series:							
	ScFe90	0.10	flux	1373 → 973	6 K/h	0.0001	73
	ScFe75	0.18	flux	1373 → 973	6 K/h	0.0001	73
	ScFe80	0.44	flux	1373 → 973	6 K/h	0.0001	73
	ScFe70	0.26	flux	1373 → 973	6 K/h	0.0001	69
	ScFe50b	0.29	flux	1373 → 973	6 K/h	0.0001	70
	ScFe50	0.43	flux	1373 → 973	6 K/h	0.0001	77
	ScFe40	0.62	flux	1373 → 973	6 K/h	0.0001	70
	ScFe25	0.91	flux	1373 → 973	6 K/h	0.0001	70
	ScFe20	0.94	flux	1373 → 973	6 K/h	0.0001	70
	ScFe10	0.98	flux	1373 → 973	6 K/h	0.0001	72
	LiSc2	1.00	flux	1373 → 973	6 K/h	0.0001	72
	ScPx	1.00	HP	1573	–	2.5	65
$Li(Sc_{1-x}In_x)Si_2O_6$ solid solution series:							
	LiIn10	0.06	flux	1373 → 973	6 K/h	0.0001	70
	LiIn25	0.20	flux	1373 → 973	6 K/h	0.0001	70
	LiIn35	0.26	flux	1373 → 973	6 K/h	0.0001	70
	LiIn50	0.30	flux	1373 → 973	6 K/h	0.0001	70
	LiIn65	0.55	flux	1373 → 973	6 K/h	0.0001	74
	LiIn90	0.82	flux	1373 → 973	6 K/h	0.0001	71
	LiIn100	1.00	flux	1373 → 973	6 K/h	0.0001	70

HP = high-pressure experiments; flux = high temperature solvent growth using Li_2MoO_4 as a solvent (flux to nutrient = 10 : 1);
x = actual composition from refinement of the M1 site;
rate = cooling rate.

ing materials were filled into small platinum tubes, tightly welded and subjected to a temperature of 1573 K and a pressure of 2.5 GPa over a period of 3–4 days in an in-house built Piston-cylinder-apparatus. These experiments lead to a few milligrams of small prismatic single crystals up to 0.07 mm in length for Me^{3+} = Al, Ga, Sc and up to 0.15 mm for $LiFeSi_2O_6$.

Single crystals of $LiCrSi_2O_6$, $LiScSi_2O_6$ (for comparison with the samples grown at high pressure), $LiInSi_2O_6$ and compounds of the $Li(Fe_{1-x}Sc_x)Si_2O_6$ and of the $Li(Sc_{1-x}In_x)Si_2O_6$ solid solution series (Table 1) were prepared from stoichiometric mixtures of $LiCO_3$, Cr_2O_3, Sc_2O_3, In_2O_3 or Fe_2O_3 and SiO_2 in the desired composition by using a high-temperature solution (flux) growth technique. One part by weight of the finely ground starting material was mixed with ten parts by weight of the high-temperature solvent Li_2MoO_4 and filled into an open platinum crucible, which was then closed with a crimped Pt-cover. The mixture was slowly heated to 1373 K, equilibrated at this temperature for 24 hours and subsequently cooled down to 973 K at a rate of 6 K/hour. Li_2MoO_4 can easily be removed from the product by dissolution in boiling water. The resulting products consisted of prismatic to needle-shaped clinopyroxene crystals up to $0.05 \times 0.05 \times 3.5$ mm in size and small amounts of $Li_2Si_2O_5$. Using ^{57}Fe Mössbauer spectroscopy, selected samples were checked for the valence of iron and in all cases Fe^{3+} was found exclusively.

All attempts to substitute cations larger than In^{3+}, e.g. Y^{3+} on the M1 site, both by high-temperature/high-pressure experiments and by flux growth techniques failed. Also, we were not able to obtain single crystals of the $LiAlSi_2O_6$–$LiGaSi_2O_6$ solid solution.

The sample of $LiVSi_2O_6$ was synthesised hydrothermally at 973 K and a pressure of 0.4 GPa from a stoichiometric mixture of Li_2CO_3, V_2O_3 and SiO_2. The sample material together with ≈10 wt% H_2O was filled into an $Ag_{70}Pd_{30}$ tube, tightly welded and placed in a cold-sealed pressure vessel. The redox-conditions of the pressure-vessel (close to the nickel/nickeloxide solid state oxygen buffer) were used to control the oxidation state of V^{3+} during the experiment. The product of the run consisted of aggregates of grass-green needles of $LiVSi_2O_6$, about $0.02 \times 0.02 \times 2.0$ mm in size.

Selected single crystals from the synthesis experiments with a minimum of twinning (less than 5% of the second individual, see below) were used for subsequent structure refinement by X-ray diffraction. Although more than 20 crystals had been tested for each composition, not a single one is absolutely free of polysynthetic twinning. More detailed comments on this twinning are given in Redhammer and Roth (2002). The single-crystal X-ray diffraction data sets were collected on an imaging-plate diffractometer system (Stoe-IPDS, MoK_α radiation, pyrolytic graphite monochromator). The programs X-SHAPE (Stoe & Cie, 1996) and SHELXL (Sheldrick, 1997) were used for empirical absorption correction via reflection intensity equivalents and structure refinement, respectively. The chemical composition of the samples was determined by M1 site refinement in single crystal structure analysis. It was assumed, that the M2 and the T sites are fully and exclusively occupied by lithium and silicon, respectively. Lattice parameters were refined at 298 K from powder X-ray diffraction data (Siemens D500, CuK_α radiation, secondary graphite monochromator) of ground single crystals, using Le-Bail whole pattern refinements as implemented in the program FULLPROF (Rodriguez-Carvajal, 2001). Data were collected between 10° and 110° 2θ, and silicon (a = 5.43094 Å at 298 K) was used as an internal standard.

Results and discussion

With the exception of $LiCrSi_2O_6$, all clinopyroxenes investigated here, show *C2/c* symmetry at room temperature (295 ± 2 K), $LiCrSi_2O_6$ has space group $P2_1/c$. At 330 K, $LiCrSi_2O_6$ transforms to the *C2/c* high-temperature structure (Redhammer, 2001; Redhammer and Roth 2004). For the sake of comparison (same space group for all compounds) the structural data for $LiCrSi_2O_6$ are those of the *C2/c* phase at a temperature of 335(1) K, well above the phase transition. For $LiScSi_2O_6$, single-crystal results from high-temperature/high-pressure experiments and from flux growth experiments are compared to each other. The structures are identical within experimental error. Thus we assume that structural variations within the Li-clinopyroxene series solely depend on different chemistries and are not affected by different preparation techniques.

Details on data collection, crystallographic and refinement parameters for selected samples are given in Table 2. Fractional atomic coordinates and equivalent isotropic atomic displacement parameters can be found in Table 3 and selected bond lengths, bond angles and polyhedral distortion parameters are listed in Table 4. The structural variations within the Li-clinopyroxene series are a consequence of the substitutions on the octahedral M1 site. The average M1–O bond length is positively correlated with the ionic radii (Fig. 2) for octahedral coordination as given by Shannon and Prewitt (1969). Except for Figure 2, all structural variations in the $LiMe^{3+}Si_2O_6$ series will be discussed in terms of the average M1–O bond lengths.

It should be recalled that $LiGaSi_2O_6$ (T_p = 286 K, Sato et al. 1997) and $LiCrSi_2O_6$ are close to the $P2_1/c \rightarrow C2/c$

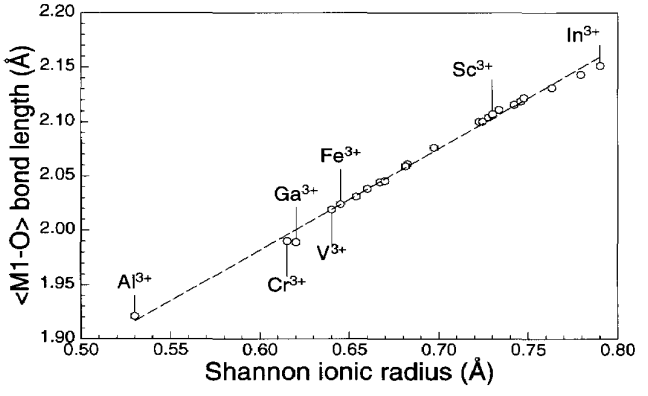

Fig. 2. Average octahedral bond lengths *vs.* the ionic radius (Shannon and Prewitt, 1969) for octahedral coordination in the $LiMe^{3+}Si_2O_6$ series. Error bars are smaller than the symbols; a linear regression line is fitted to the data as a guide to the eye.

Table 2. Experimental details for the X-ray data collection and crystallographic parameters for selected samples of the $LiMe^{3+}Si_2O_6$ series; all samples exhibit space group C2/c, $Z = 4$, absorption correction via equivalents.

	LiAl	LiGa	LiCr	LiV	LiFe	ScFe90	ScFe75	ScFe70	ScFe50
Crystal data									
T (K)	295(2)	295(2)	335(2)	295(2)	295(2)	295(2)	295(2)	295(2)	295(2)
a (Å)	9.474(4)	9.593(3)	9.570(3)	9.657(4)	9.664(2)	9.678(4)	9.686(4)	9.704(4)	9.723(3)
b (Å)	8.390(4)	8.584(2)	8.582(4)	8.623(4)	8.660(2)	8.697(2)	8.718(2)	8.737(2)	8.795(3)
c (Å)	5.219(3)	5.284(3)	5.268(2)	5.287(2)	5.293(1)	5.300(2)	5.308(2)	5.312(2)	5.322(1)
β (°)	110.07(5)	110.22(4)	110.18(4)	110.15(5)	110.19(3)	110.15(4)	110.20(4)	110.20(4)	110.25(3)
V (Å^3)	389.66	408.21	406.03	413.32	415.78	418.79	420.68	422.66	427.00
M_r	186.1	228.84	211.12	210.06	214.97	213.61	213.07	212.11	210.34
D_{calc} (g/cm^3)	3.172	3.724	3.454	3.376	3.434	3.388	3.364	3.330	3.275
μ (mm^{-1})	1.07	7.27	3.35	2.92	4.14	3.88	3.77	3.60	3.27
Colour	transparent	transparent	emerald-green	grass-green	yellow-green	yellow-green	yellow green	yellow green	pale yellow-green
shape	prism-plate	cuboid	prism	needle	prism	prism	cuboid	cuboid	prism
size max (mm)	0.21	0.15	0.16	0.11	0.15	0.14	0.15	0.16	0.14
Data collection									
$2\theta_{max}$ (°)	56.11	56.21	56.11	56.28	55.84	55.75	55.99	55.89	55.94
hkl range: h	$-12 \rightarrow 12$	$-12 \rightarrow 11$	$-12 \rightarrow 12$	$-12 \rightarrow 12$	$-12 \rightarrow 12$	$-12 \rightarrow 12$	$-12 \rightarrow 12$	$-12 \rightarrow 12$	$-12 \rightarrow 12$
k	$-9 \rightarrow 10$	$-11 \rightarrow 11$	$-11 \rightarrow 10$	$-11 \rightarrow 11$	$-11 \rightarrow 11$	$-11 \rightarrow 11$	$-11 \rightarrow 11$	$-11 \rightarrow 11$	$-11 \rightarrow 11$
l	$-6 \rightarrow 6$	$-6 \rightarrow 6$	$-6 \rightarrow 6$	$-6 \rightarrow 6$	$-6 \rightarrow 6$	$-6 \rightarrow 6$	$-6 \rightarrow 6$	$-6 \rightarrow 6$	$-6 \rightarrow 6$
$T_{min.}$	0.74	0.30	0.38	0.63	0.42	0.40	0.56	0.48	0.32
$T_{max.}$	0.92	0.43	0.67	0.68	0.60	0.51	0.60	0.56	0.49
$N_{measured}$	1857	1811	1536	1665	3173	2001	2035	2101	2335
$N_{independent}$	444	489	275	397	501	459	484	489	503
R_{int} (%)	2.86	3.80	6.77	3.52	2.84	4.39	2.29	2.51	3.41
Refinement									
$N_{parameters}$	48	48	48	47	47	49	49	49	49
$R_1 > 4\sigma$ (%)	1.88	1.82	3.85	2.33	1.49	1.76	1.63	1.67	1.94
R_1 all (%)	2.57	3.03	4.22	3.44	1.75	1.93	1.89	2.16	2.19
$wR_2 > 4\sigma$ (%)	5.24	3.63	9.27	5.39	4.95	4.90	4.26	4.41	5.82
wR_2 all (%)	5.63	3.82	10.71	5.78	5.68	6.42	5.92	7.31	7.50
G.O.F.	1.296	0.996	1.332	1.080	1.373	1.512	1.570	1.769	1.507
$\Delta\sigma_{min}$ (e/Å^3)	−0.33	−0.41	−0.67	−0.41	−0.32	−0.37	−0.43	−0.34	−0.35
$\Delta\sigma_{max}$ (e/Å^3)	0.44	0.44	0.48	0.50	0.36	0.34	0.31	0.33	0.35
weight w (a, b)	0.0400	0.0154	0.0686	0.0337	0.0296/0.381	0.0231/0.501	0.0270/0.202	0.0309	0.0395/0.044
Extinction (x)	0.0515	0.0063	0.454	–	–	–	–	–	–

$T_{min.}$ = minimum transmission, $T_{max.}$ = maximum transmission,
$R_1 = \sum ||F_o| - |F_c|| / \sum |F_o|$, $wR_2 = \{\sum [w(F_o^2 - F_c^2)^2] / \sum [w(F_o^2)^2]\}^{1/2}$, $w = 1/[\sigma^2(F_o^2) + (aP)^2 + bP]$ where $P = [2F_c^2 + \max(F_o^2, 0)]/3$,
Extinction: F_c is multiplied by the overall scale factor $k[1 + 0.001xF_c^2\lambda^3/\sin(2\Theta)]^{-1/4}$ where the extinction parameter x is refined.

phase transition. Particularly the lattice parameters change drastically in the vicinity of the phase transition. Thus, the small deviations of the Ga^{3+} and Cr^{3+} data from the linear plot for the other $LiMe^{3+}Si_2O_6$ clinopyroxenes should also be seen in the light of the closeness of the $P2_1/c \rightarrow C2/c$ phase transition.

Lattice parameters

Figure 3 depicts the changes in lattice parameters within the $LiMe^{3+}Si_2O_6$ series. The most remarkable data course is the a-lattice parameter for the $LiSc_{1-x}In_xSi_2O_6$ series. While a increases steadily from $LiAlSi_2O_6$ to $LiScSi_2O_6$, no changes are observed for the $LiSc_{1-x}In_xSi_2O_6$ series, although the smaller Sc^{3+} ($r^{VI} = 0.73$ Å) is replaced by the larger In^{3+} ($r^{VI} = 0.79$ Å, Shannon and Prewitt, 1969). Within this solid-solution series, the increase of b and c with increasing ⟨M1—O⟩ is also smaller than the changes for the other compositions. A deviation from a linear variation of lattice parameters *vs.* ⟨M1—O⟩ is evident for c and the monoclinic angle β.

The octahedral M1 site

The variations of structural parameters in the $LiMe^{3+}Si_2O_6$ clinopyroxenes are dominated by the M1 site. The ionic radius for octahedral coordination ranges between 0.53 Å for Al^{3+} and 0.79 Å for In^{3+} (Shannon and Prewitt, 1969).

Table 2. (Continued)

	ScFe40	ScFe25	ScPx	LiSc2	LiIn25	LiIn50	LiIn65	LiIn90	LiIn100
Crystal data									
T (K)	295(2)	295(2)	295(2)	295(2)	295(2)	295(2)	295(2)	295(2)	295(2)
a (Å)	9.747(3)	9.794(4)	9.805(3)	9.805(3)	9.801(3)	9.801(3)	9.802(2)	9.806(2)	9.807(2)
b (Å)	8.846(3)	8.917(2)	8.949(2)	8.949(2)	8.965(2)	8.985(2)	9.005(3)	9.035(3)	9.055(2)
c (Å)	5.335(1)	5.351(2)	5.358(2)	5.358(2)	5.361(1)	5.366(1)	5.370(1)	5.377(1)	5.383(1)
β (°)	110.28(3)	110.36(4)	110.39(3)	110.39(4)	110.38(3)	110.38(2)	110.41(3)	110.46(3)	110.49(2)
V (Å^3)	431.45	438.11	440.64	440.64	441.57	442.94	444.22	446.33	447.77
M_r	208.17	204.89	204.08	204.08	218.05	224.17	242.50	260.84	273.94
D_{calc} (g/cm^3)	3.205	3.106	3.076	3.076	3.280	3.361	3.626	3.882	4.064
μ (mm^{-1})	2.87	2.30	2.16	2.16	2.89	3.20	4.16	5.09	5.76
Colour	pale yellow	pale yellow	white transp.	white transp.	white transp.	white transp.	white transp.	white transp.	white transp.
shape	cuboid	prism	prism	prism	prism	prism	cuboid	prism	prism
size max (mm)	0.16	0.24	0.16	0.23	0.20	0.28	0.17	0.23	0.16
Data collection									
$2\theta_{max}$ (°)	55.93	56.16	55.52	56.25	56.20	55.89	56.08	56.01	55.84
hkl range: h	$-12 \rightarrow 12$	$-12 \rightarrow 12$	$-12 \rightarrow 12$	$-12 \rightarrow 12$	$-12 \rightarrow 12$	$-12 \rightarrow 12$	$-12 \rightarrow 12$	$-12 \rightarrow 12$	$-12 \rightarrow 12$
k	$-11 \rightarrow 11$	$-11 \rightarrow 11$	$-11 \rightarrow 11$	$-11 \rightarrow 11$	$-11 \rightarrow 11$	$-11 \rightarrow 11$	$-11 \rightarrow 11$	$-11 \rightarrow 11$	$-11 \rightarrow 11$
l	$-6 \rightarrow 6$	$-6 \rightarrow 6$	$-6 \rightarrow 6$	$-7 \rightarrow 7$	$-7 \rightarrow 7$	$-6 \rightarrow 7$	$-6 \rightarrow 6$	$-7 \rightarrow 7$	$-6 \rightarrow 6$
$T_{min.}$	0.62	0.58	0.58	0.59	0.45	0.42	0.52	0.35	0.37
$T_{max.}$	0.66	0.68	0.72	0.79	0.69	0.67	0.63	0.54	0.52
$N_{measured}$	2087	2122	2093	2129	2116	2268	2142	2117	2375
$N_{independent}$	487	516	522	538	533	514	495	535	500
R_{int} (%)	3.18	2.29	2.73	3.12	2.80	5.66	2.73	4.56	3.28
Refinement									
$N_{parameters}$	49	49	49	48	50	50	49	50	47
$R_1 > 4\sigma$ (%)	2.58	1.75	1.54	1.94	2.08	2.88	1.38	1.66	1.39
R_1 all (%)	3.15	1.98	1.87	2.40	2.32	3.25	1.64	1.98	1.70
$wR_2 > 4\sigma$ (%)	6.52	4.66	4.23	5.22	5.18	6.78	3.26	4.17	3.61
wR_2 all (%)	7.71	7.26	5.54	6.29	6.36	7.13	3.52	4.90	3.66
G.O.F.	1.228	1.715	1.470	1.318	1.411	1.810	1.268	1.384	1.106
$\Delta\sigma_{min}$ (e/Å^3)	−0.51	−0.29	−0.24	−0.31	−0.61	−0.86	−0.26	−0.97	−0.85
$\Delta\sigma_{max}$ (e/Å^3)	0.44	0.33	0.30	0.47	0.45	1.03	0.29	0.54	0.44
weight w (a, b)	0.0473	0.0352/0.015	0.0236/0.316	0.0342/0.053	0.0365/0.059	0.0210/0.989	0.0138/0.566	0.0217	0.0213/0.355
Extinction (x)	–	–	0.0198	0.0647	0.0261	0.0173	–	0.0029	–

see above

The substitution of cations larger than In^{3+} (e.g. Y^{3+}) was not possible. The edge-sharing zig-zag chain of M1 sites represents a very robust unit. Changes within it force rearrangements in the (average) geometry of the corner-sharing tetrahedral chain and within the M2–O polyhedra.

The variation of individual M1–O bond lengths *vs.* ionic radius (Fig. 4a) is not uniform. The most pronounced increase is observed for the four M1–O bonds within the equatorial plane of the octahedron, the M1–O1(a2, b2) bonds to the apex oxygen atoms exhibit a smaller increase. With increasing size of the large cation, the octahedra become more and more tetragonally compressed. This is also expressed by O1(a2)–M1–O1(b2) bond angles, which linearly decrease from 174.7(1)° in $LiAlSi_2O_6$ to 168.1(1)° in $LiInSi_2O_6$, except for Cr^{3+} and V^{3+} samples (Table 4). The latter two have shorter M1–O1(a1, b1), somewhat longer M1–O2(c1, d1) bonds and more ideal, i.e. closer to 180°, O1(a2)–M1–O1(b2) and O1–M1–O2 bond angles. Thus the octahedra in these two compounds appear to be more regular in terms of the octahedral angle variance (OAV[1], Renner and Lehmann, 1986) and are distinctly different from the overall trend observed for the other samples (Fig. 4b). The very similar behaviour has been described very recently by

[1] $OAV = \sum_{i=1}^{12} (\Theta_i - 90°)^2/11$ with Θ_i = O–M–O bonding angle (Renner and Lehmann, 1986).

Table 3. Atomic coordinates and equivalent isotropic displacement parameters for selected samples of the $LiMe^{3+}Si_2O_6$ series.

		LiAl	LiGa	LiCr	LiV	LiFe(1)	ScFe90	ScFe75	ScFe70	ScFe50
M2 (Li)	x	0.0	0.0	0.0	0.0	0.0	0.0	0.0	0.0	0.0
	y	0.2746(4)	0.2654(9)	0.2656(9)	0.2678(8)	0.2628(5)	0.2605(5)	0.2601(5)	0.2600(5)	0.2586(6)
	z	1/4	1/4	1/4	1/4	1/4	1/4	1/4	1/4	1/4
	U_{eq}	0.0154(7)	0.0148(16)	0.0235(16)	0.0124(12)	0.0143(8)	0.0182(9)	0.0181(8)	0.0190(9)	0.0192(10)
M1	x	0.0	0.0	0.0	0.0	0.0	0.0	0.0	0.0	0.0
	y	0.90674(7)	0.90159(6)	0.90861(6)	0.90589(7)	0.89835/3)	0.89809(3)	0.89785(3)	0.89764(3)	0.89696(4)
	z	1/4	1/4	1/4	1/4	1/4	1/4	1/4	1/4	1/4
	U_{eq}	0.0035(2)	0.0023(1)	0.0094(3)	0.0023(1)	0.0035(1)	0.0040(1)	0.0040(1)	0.0038(1)	0.0049(2)
	Occ.	1.00 Al	1.00 Ga	1.00 Cr	1.00 V	1.00 Fe	0.127(3) Fe	0.177(6) Fe	0.261(6) Fe	0.426(7) Fe
	Occ.	–	–	–	–	–	0.873(3) Sc	0.826(6) Sc	0.739(6) Sc	0.573(7) Sc
T (Si)	x	0.29413(3)	0.29654(6)	0.29812(9)	0.29678(6)	0.29611(5)	0.29646(5)	0.29663(4)	0.29677(4)	0.29733(5)
	y	0.09354(4)	0.09102(9)	0.09152(7)	0.09058(8)	0.08949(5)	0.08933(4)	0.08916(8)	0.08900(4)	0.08848(5)
	z	0.25599(7)	0.2610(1)	0.2619(2)	0.2685(1)	0.26580(8)	0.26642(9)	0.26702(8)	0.26763(9)	0.26976(10)
	U_{eq}	0.0032(1)	0.0020(2)	0.0099(3)	0.0024(2)	0.0033(1)	0.0045(1)	0.0044(1)	0.0045(2)	0.0058(2)
O1	x	0.1096(1)	0.1135(2)	0.1153(2)	0.1170(2)	0.1160(1)	0.1162(1)	0.1166(1)	0.1171(1)	0.1180(1)
	y	0.0825(1)	0.0838(2)	0.0846(2)	0.0858(2)	0.0846(1)	0.0846(1)	0.0846(1)	0.0845(1)	0.0844(1)
	z	0.1404(2)	0.1441(3)	0.1474(5)	0.1553(4)	0.1497(2)	0.1499(2)	0.1505(2)	0.1507(2)	0.1520(3)
	U_{eq}	0.0044(2)	0.0037(4)	0.0109(6)	0.0038(4)	0.0046(2)	0.0059(3)	0.0059(2)	0.0062(3)	0.0072(3)
O2	x	0.3647(1)	0.3653(2)	0.3676(2)	0.3689(2)	0.3662(1)	0.3667(1)	0.3671(1)	0.3673(1)	0.3681(1)
	y	0.2669(1)	0.2617(2)	0.2616(3)	0.2599(2)	0.2584(1)	0.2578(1)	0.2572(1)	0.2565(1)	0.2547(1)
	z	0.3004(2)	0.3241(4)	0.3241(4)	0.3273(4)	0.3252(2)	0.3267(3)	0.3281(3)	0.3294(3)	0.3333(3)
	U_{eq}	0.0073(2)	0.0073(4)	0.0150(5)	0.0072(4)	0.0081(2)	0.0097(3)	0.0097(2)	0.0099(3)	0.0113(3)
O3	x	0.35650(9)	0.3568(2)	0.3573(2)	0.3557(2)	0.3557(1)	0.3558(1)	0.3556(1)	0.3554(1)	0.3554(1)
	y	−0.0133(1)	−0.0003(2)	−0.0012(2)	−0.0023(3)	−0.0013(1)	−0.0010(1)	−0.0002(1)	0.0066(1)	0.0021(2)
	z	0.0585(2)	0.0497(3)	0.0513(5)	0.0568(3)	0.0553(2)	0.0550(3)	0.0549(3)	0.0548(3)	0.0547(3)
	U_{eq}	0.0069(2)	0.0064(4)	0.0165(5)	0.0077(4)	0.0084(2)	0.0105(3)	0.0105(3)	0.0108(3)	0.0121(3)

		ScFe40	ScFe25	ScPx	LiSc2	LiIn25	LiIn50	LiIn65	LiIn90	LiIn100
M2 (Li)	x	0.0	0.0	0.0	0.0	0.0	0.0	0.0	0.0	0.0
	y	0.2571(7)	0.2566(4)	0.2567(4)	0.2568(6)	0.2545(6)	0.2533(9)	0.2523(6)	0.2501(8)	0.2492(7)
	z	1/4	1/4	1/4	1/4	1/4	1/4	1/4	1/4	1/4
	U_{eq}	0.0209(13)	0.0192(7)	0.0180(8)	0.0170(9)	0.0181(9)	0.0180(15)	0.0181(12)	0.0164	0.0132(14)
M1	x	0.0	0.0	0.0	0.0	0.0	0.0	0.0	0.0	0.0
	y	0.89631(5)	0.89523(3)	0.89509(3)	0.89502(5)	0.89436(3)	0.89401(4)	0.89341(3)	0.89288(3)	0.89257
	z	1/4	1/4	1/4	1/4	1/4	1/4	1/4	1/4	1/4
	U_{eq}	0.0075(2)	0.0046(1)	0.0030(1)	0.0033(2)	0.00308	0.0037(2)	0.0032(1)	0.0028(1)	0.0016(1)
		0.385(4) Fe	0.087(3) Fe	–	–	0.203 (3) In	0.289(2) In	0.553(2) In	0.815(3) In	1.00 In
		0.614(4) Sc	0.913(3) Sc	1.00 Sc	1.00 Sc	0.787 (3) Sc	0.710 (2) Sc	0.447(2) Sc	0.185(3) Sc	–
T (Si)	x	0.29783(6)	0.29873(3)	0.29888(3)	0.29885(5)	0.29959(5)	0.29983(7)	0.30044(5)	0.30114(6)	0.30125(6)
	y	0.08790(6)	0.08703(4)	0.08677(4)	0.08687(5)	0.08650(5)	0.08636(8)	0.08581(5)	0.08114(8)	0.08513(7)
	z	0.2721(1)	0.27668(7)	0.27774(7)	0.27779(8)	0.27812(9)	0.2782(1)	0.2786(1)	0.2794(1)	0.2795(2)
	U_{eq}	0.0083(2)	0.0046(1)	0.0029(1)	0.0033(2)	0.0038(1)	0.0049(2)	0.0039(1)	0.0039(2)	0.0017(1)
O1	x	0.1189(2)	0.12042(8)	0.12081(9)	0.1208(1)	0.12114(1)	0.1215(2)	0.1221(1)	0.1223(2)	0.1225(2)
	y	0.0842(2)	0.08370(8)	0.08338(9)	0.0834(1)	0.0832(1)	0.0833(2)	0.0832(1)	0.0828(2)	0.0829(2)
	z	0.1541(4)	0.1572(2)	0.1578(2)	0.1580(2)	0.1590(2)	0.1596(4)	0.1606(3)	0.1618(4)	0.1627(4)
	U_{eq}	0.0097(4)	0.0060(2)	0.0044(2)	0.0044(3)	0.0054(3)	0.0058(4)	0.0054(3)	0.0053(4)	0.0034(4)
O2	x	0.3687(2)	0.37025(8)	0.3706(1)	0.3705(1)	0.3709(1)	0.3711(2)	0.3715(1)	0.3716(2)	0.3716(2)
	y	0.2526(2)	0.24952(9)	0.2490(1)	0.2490(1)	0.2478(1)	0.2472(2)	0.2465(2)	0.2453(2)	0.2444(2)
	z	0.3371(4)	0.3432(2)	0.3445(2)	0.3446(2)	0.3494(2)	0.3518(4)	0.3566(3)	0.3616(3)	0.3639(4)
	U_{eq}	0.0136(4)	0.0096(2)	0.0078(2)	0.0079(3)	0.0088(2)	0.0097(4)	0.0092(3)	0.0080(4)	0.0056(4)
O3	x	0.3549(2)	0.35470(8)	0.35442(9)	0.3544(1)	0.3545(1)	0.3545(2)	0.3544(1)	0.3542(2)	0.3541(2)
	y	0.0032(2)	0.0053(1)	0.0054(1)	0.0054(2)	0.0088(2)	0.0096(2)	0.0126(2)	0.0150(2)	0.0165(2)
	z	0.0553(4)	0.0570(2)	0.0575(2)	0.0574(3)	0.0547(3)	0.0533(4)	0.0504(3)	0.0479(3)	0.0479(4)
	U_{eq}	0.0152(4)	0.0109(2)	0.0093(2)	0.0096(3)	0.0102(3)	0.0116(4)	0.0096(3)	0.0085(7)	0.0060(4)

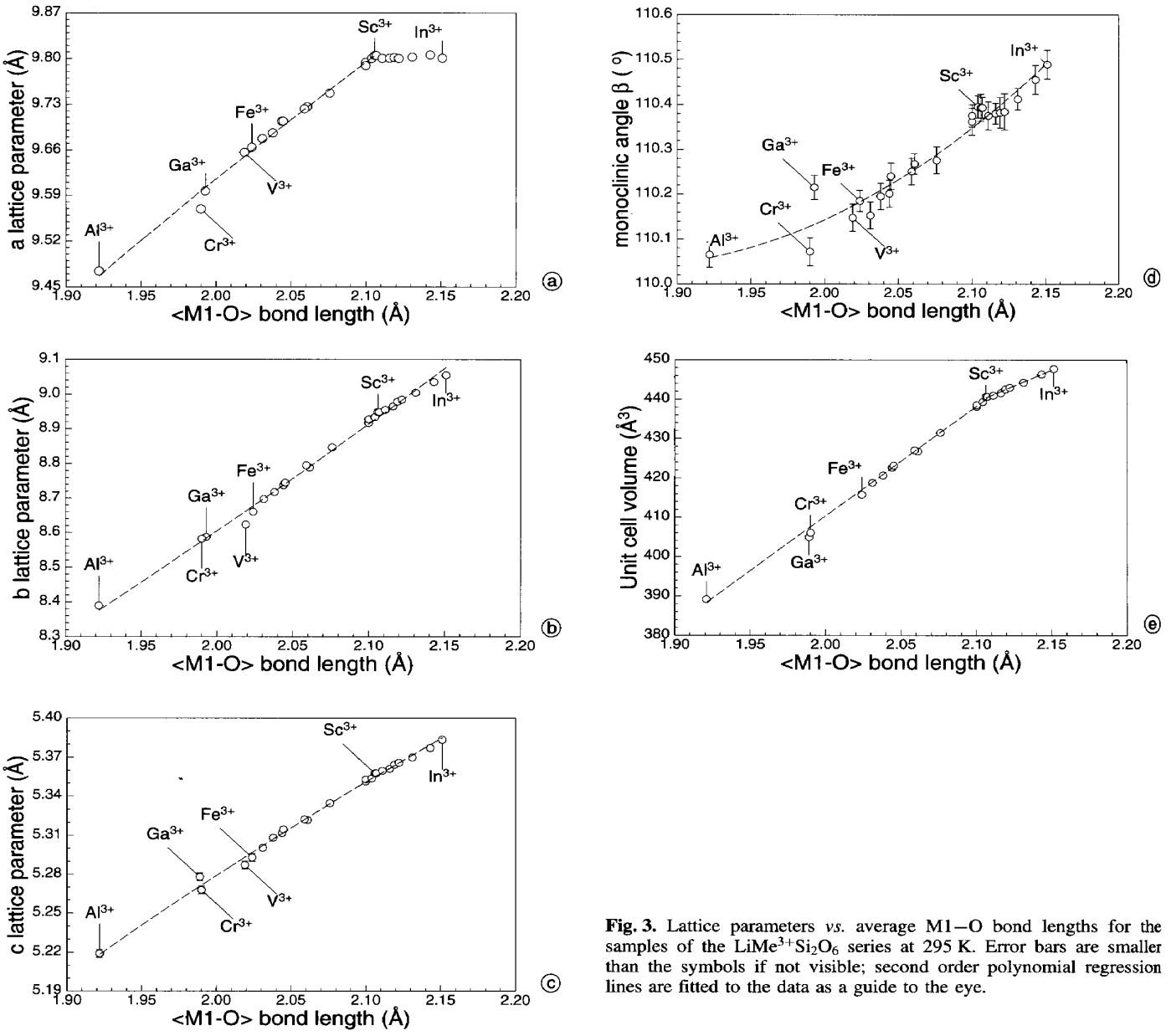

Fig. 3. Lattice parameters *vs.* average M1—O bond lengths for the samples of the $LiMe^{3+}Si_2O_6$ series at 295 K. Error bars are smaller than the symbols if not visible; second order polynomial regression lines are fitted to the data as a guide to the eye.

Redhammer, Ohashi and Roth (2003) for the $NaM^{3+}Si_2O_6$ series. When plotting the OAV *vs.* the average M1—O bond lengths (or the M1 ionic radius) for the $NaM^{3+}Si_2O_6$ series, compounds with M^{3+} = Cr, V, Mn and Ti significantly deviate from the trend defined by the Al—Ga—Fe—Sc samples. The deviation of individual bond lengths from their average value (BLD[2], Renner and Lehmann, 1986) is rather large but typical for the Li-clinopyroxenes and amounts to 3.4% in $LiAlSi_2O_6$. The BLD (Fig. 4c) steadily decreases — with a discontinuity at $LiFeSi_2O_6$ — towards $LiInSi_2O_6$ (2.3%). This discontinuity might be associated with the transition from the "S" to the "O" conformation of the tetrahedral chains.

As noted above, $LiCrSi_2O_6$ and $LiVSi_2O_6$ deviate from the Al—Ga—Fe—Sc series. This also is evident, when plotting e.g. the average M1—O1 bond lengths *vs.* the M1—M1 interatomic distance or *vs.* the O1—M1—O1 bond angles (Fig 4d). Data for $LiTiSi_2O_6$ (Redhammer, Ohashi, Roth, preliminary results; Kopnin, Sato and Takayama-Muromachi, 2003) are included in Fig. 4d. As the O1—M1—O1 bond angles are closer to the ideal values of 90° and 180° respectively (Table 4, Fig. 4d) this is one reason for the smaller OAV in the Cr^{3+} and V^{3+} compound. The deviation of the Cr^{3+}, V^{3+} (and Ti^{3+}) composition from the other members of the $LiM^{3+}Si_2O_6$ series may be caused by the repulsion between the O1 atoms and the unpaired 3d electrons of the above mentioned transition metal ions. Ohashi, Osawa and Tsukimura (1987) and later on Redhammer et al. (2003) noted that the geometry of the M1 site can also be characterized by plotting the M1—M1 interatomic distance *vs.* the mean

[2] $\mathrm{BLD} = \frac{100}{n} \sum_{i=1}^{n} \frac{|(\mathrm{X-O})_i - (\langle \mathrm{X-O} \rangle)|}{(\langle \mathrm{X-O} \rangle)}$ %, n = amount of cation-anion bonds and X—O = cation-anion (oxygen) distance (Renner and Lehmann, 1986).

Table 4. Selected bond distances (Å) and angles (°) and polyhedral distortion parameters for selected samples of the $LiMe^{3+}Si_2O_6$ series.

Sample/ Temperature (K)	LiAl 298	LiGa 298	LiCr 336	LiV 298	LiFe 298	ScFe90 298	ScFe75 298	ScFe70 298	ScFe50 298
M2–O2	2.282(2)	2.181(2)	2.176(2)	2.169(2)	2.178(1)	2.175(2)	2.169(3)	2.164(2)	2.147(2)
M2–O1	2.100(3)	2.078(6)	2.081(6)	2.093(6)	2.077(4)	2.073(4)	2.076(4)	2.082(4)	2.085(4)
M2–O3	2.254(2)	2.469(6)	2.445(6)	2.436(6)	2.492(4)	2.515(4)	2.529(4)	2.539(4)	2.575(4)
⟨*M2–O*⟩	*2.212*	*2.243*	*2.234*	*2.233*	*2.249*	*2.254*	*2.258*	*2.262*	*2.269*
BLD [%]	3.4(1)	6.7(1)	6.3(1)	6.1(1)	7.2(1)	7.7(1)	8.0(1)	8.2(1)	9.0(1)
M1–O2	1.822(1)	1.897(2)	1.919(2)	1.926(2)	1.910(1)	1.918(1)	1.924(1)	1.932	1.950
M1–O1	1.946(1)	1.992(2)	2.002(3)	2.051(2)	2.028(1)	2.034(1)	2.040(1)	2.043	2.054
M1–O1	1.997(1)	2.091(2)	2.050(2)	2.079(2)	2.135(1)	2.142(1)	2.149(1)	2.156	2.173
⟨*M1–O*⟩	*1.922*	*1.993*	*1.990*	*2.019*	*2.024*	*2.031*	*2.038*	*2.044*	*2.059*
BLD (%)	3.5(1)	3.3(1)	2.4(1)	3.1(1)	3.8(1)	3.7(1)	3.7(1)	3.7(1)	3.7(1)
⟨*O–O*⟩	*2.714*	*2.810*	*2.812*	*2.850*	*2.853*	*2.862*	*2.871*	*2.879*	*2.901*
$\langle O-O\rangle_s = e_s$	*2.623*	*2.698*	*2.708*	*2.751*	*2.747*	*2.756*	*2.763*	*2.771*	*2.789*
$\langle O-O\rangle_u = e_u$	*2.778*	*2.890*	*2.886*	*2.920*	*2.928*	*2.939*	*2.949*	*2.957*	*2.981*
e_u/e_s	1.059	1.071	1.066	1.062	1.066	1.066	1.067	1.067	1.069
ELD (%)	3.4(1)	3.8(1)	3.5(1)	3.3(1)	3.3(1)	3.3(1)	3.3(1)	3.3(1)	3.2(1)
M1–M1 (intra)	3.043(1)	3.129(1)	3.065(1)	3.102(1)	3.179(1)	3.188(1)	3.196(1)	3.202(1)	3.220(1)
M1–M1 (inter)	5.254(1)	5.273(1)	5.343(1)	5.287(1)	5.304(1)	5.314(1)	5.317(1)	5.325(1)	5.333(1)
O1–M1–O1	84.8(1)	83.2(1)	85.1(1)	83.5(1)	81.7(1)	81.6(1)	81.5(1)	81.5(1)	81.3(1)
O1–M1–O1 ×2	79.0(1)	79.8(1)	81.7(1)	82.6(1)	80.5(1)	80.5(1)	80.6(1)	80.7(1)	80.8(1)
O1–M1–O1 ×2	97.0(1)	94.8(1)	95.8(1)	94.4(1)	93.3(1)	93.1(1)	92.9(1)	92.7(1)	92.2(1)
O1–M1–O1	174.7(1)	172.7(1)	176.7(1)	176.0(1)	171.8(1)	171.5(1)	171.4(1)	171.3(1)	170.9(1)
O1–M1–O2 ×2	88.5(1)	87.9(1)	88.3(1)	88.1(1)	88.7(1)	88.9(1)	89.0(1)	89.0(1)	89.3(1)
O1–M1–O2 ×2	91.6(1)	89.5(1)	88.7(1)	89.1(1)	89.9(1)	89.8(1)	89.7(1)	89.7(1)	89.5(1)
O1–M1–O2 ×2	91.8(1)	95.1(1)	93.9(1)	94.5(1)	95.4(1)	95.6(1)	95.8(1)	95.9(1)	96.5(1)
O1–M1–O2 ×2	167.8(1)	169.2(1)	171.9(1)	171.9(1)	169.2(1)	169.4(1)	169.6(1)	169.8(1)	170.1(1)
O2–M1–O2	99.9(1)	101.7(1)	97.9(1)	98.4(1)	101.3(1)	101.0(1)	100.8(1)	100.7(1)	100.2(1)
OAV [°]	50.6(5)	51.5(5)	31.4(5)	30.1(5)	49.7(5)	49.3(5)	49.0(5)	48.3(5)	48.2(5)
Si–O2	1.585(1)	1.594(1)	1.590(2)	1.602(2)	1.599(1)	1.601(1)	1.601(1)	1.601(1)	1.601(1)
Si–O3	1.622(1)	1.624(1)	1.618(2)	1.622(2)	1.624(1)	1.627(1)	1.626(2)	1.627(1)	1.629(1)
Si–O3	1.630(1)	1.628(1)	1.628(2)	1.630(2)	1.628(1)	1.629(1)	1.631(2)	1.631(1)	1.631(1)
Si–O1	1.644(1)	1.647(1)	1.643(2)	1.630(2)	1.636(1)	1.638(1)	1.637(1)	1.637(1)	1.637(1)
⟨*Si–O*⟩	*1.620*	*1.623*	*1.620*	*1.621*	*1.622*	*1.624*	*1.624*	*1.624*	*1.625*
BLD [%]	1.1(1)	0.901(1)	0.972(1)	0.586(1)	0.701(1)	0.701(1)	0.701(1)	0.708(1)	0.723(1)
O1c1–Si–O3c1	108.0(1)	108.5(1)	108.1(1)	108.4(1)	108.9(1)	109.1(1)	109.0(1)	109.0(1)	109.0(1)
O1c1–Si–O3c2	108.6(1)	108.1(1)	108.0(1)	108.5(1)	108.3(1)	108.1(1)	108.0(1)	107.9(1)	107.6(1)
O1c1–Si–O2c1	116.6(1)	115.2(1)	115.1(1)	115.6(1)	114.9(1)	115.0(1)	115.0(1)	115.1(1)	115.1(1)
O2c1–Si–O3c1	111.9(1)	111.5(1)	111.9(1)	110.5(1)	110.5(1)	110.7(1)	110.6(1)	110.5(1)	110.3(1)
O2c1–Si–O3c2	104.1(1)	104.9(1)	105.0(1)	104.9(1)	104.9(1)	104.9(1)	105.0(1)	105.1(1)	105.3(1)
O3c1–Si–O3c2	107.3(1)	108.5(1)	108.5(1)	108.8(1)	109.1(1)	109.0(1)	109.2(1)	109.2(1)	109.5(1)
TAV [°]^2	18.6(5)	12.4(5)	12.6(5)	12.3(5)	10.8(5)	11.1(5)	10.9(5)	10.9(5)	10.5(5)
τ	111.1(1)	110.6(1)	110.4(1)	110.8(1)	110.7(1)	110.7(1)	110.7(1)	110.6(1)	110.6(1)
O3–O3–O3	170.3(1)	179.9(1)	179.0(1)	178.3(1)	179.2(1)	179.2(1)	179.8(1)	179.8(1)	178.4(1)

$$\text{BLD} = \frac{100}{n}\sum_{i=1}^{n}\frac{|(\text{X}-\text{O})_i - (\langle\text{X}-\text{O}\rangle)|}{(\langle\text{X}-\text{O}\rangle)}\ \%,\ n = \text{amount of cation-anion bonds and X–O = cation-anion (oxygen) distance (Renner and Lehmann, 1986);}$$

$$\text{ELD} = \frac{100}{n}\sum_{i=1}^{n}\frac{|(\text{O}-\text{O})_i - (\langle\text{O}-\text{O}\rangle)|}{(\langle\text{O}-\text{O}\rangle)}\ \%,\ n = \text{amount of edges and (O–O) = oxygen-oxygen interatomic distance defining an edge of the octahedron;}$$

e_u/e_s = mean of the O–O interatomic distances defining unshared edges of the octahedron (e_u)/mean of the O–O interatomic distances defining the shared edges of the octahedron (e_s), Toraya (1981);

Table 4. (Continued)

Sample/ Temperature/ K	ScFe40 298	ScFe25 298	ScPx 298	LiSc2 298	LiIn25 298	LiIn50 298	LiIn65 298	LiIn90 298	LiIn100 298
M2–O2	2.132(2)	2.105(1)	2.100(1)	2.100(2)	2.079(2)	2.069(2)	2.048(2)	2.027(2)	2.018(2)
M2–O1	2.087(5)	2.103(3)	2.112(3)	2.113(4)	2.102(4)	2.095(6)	2.094(4)	2.084(6)	2.080(5)
M2–O3	2.608(5)	2.645(3)	2.651(3)	2.651(4)	2.699(4)	2.720(6)	2.759(4)	2.805(6)	2.828(5)
$\langle M2-O\rangle$	*2.276*	*2.284*	*2.288*	*2.288*	*2.293*	*2.295*	*2.300*	*2.305*	*2.309*
BLD [%]	9.7(1)	10.5(1)	10.6(1)	10.6(1)	11.8(1)	12.4(1)	13.3(1)	14.4(1)	15.0(1)
M1–O2	1.971(2)	1.998(1)	2.006(1)	2.007(1)	2.021(1)	2.029(2)	2.041(1)	2.062(2)	2.075(2)
M1–O1	2.071(2)	2.094(1)	2.100(1)	2.101(2)	2.109(1)	2.113(2)	2.121(2)	2.129(2)	2.135(2)
M1–O1	2.186(2)	2.207(1)	2.212(1)	2.212(1)	2.219(1)	2.225(2)	2.232(1)	2.237(2)	2.243(2)
$\langle M1-O\rangle$	*2.076*	*2.100*	*2.106*	*2.107*	*2.116*	*2.122*	*2.131*	*2.143*	*2.151*
BLD [%]	3.5(1)	3.4(1)	3.4(1)	3.3(1)	3.2(1)	3.2(1)	3.2(1)	2.9(1)	2.9(1)
$\langle O-O\rangle$	*2.925*	*2.958*	*2.967*	*2.968*	*2.980*	*2.989*	*3.001*	*3.016*	*3.027*
$\langle O-O\rangle_s = e_s$	*2.809*	*2.837*	*2.845*	*2.845*	*2.851*	*2.854*	*2.860*	*2.864*	*2.870*
$\langle O-O\rangle_u = e_u$	3.008	3.044	3.054	3.055	3.073	3.085	3.102	3.125	3.140
e_u/e_s	1.071	1.073	1.074	1.074	1.078	1.081	1.084	1.091	1.094
ELD [%]	3.3(1)	3.4(1)	3.4(1)	3.4(1)	3.6(1)	3.8(1)	3.9(1)	4.2(1)	4.3(1)
Fe-Fe (intra)	3.237(1)	3.263(1)	3.271(1)	3.272(1)	3.282(1)	3.290(1)	3.306(1)	3.313(1)	3.321(1)
Fe-Fe (inter)	5.344(1)	5.360(1)	5.367(1)	5.366(1)	5.362(1)	5.362(1)	5.360(1)	5.359(1)	5.359(1)
O1–M1–O1	81.0(1)	80.8(1)	80.8(1)	80.7(1)	80.6(1)	80.3(1)	80.1(1)	79.8(1)	79.6(1)
O1–M1–O1 ×2	81.0(1)	81.3(1)	81.4(1)	81.4(1)	81.4(1)	81.4(1)	81.4(1)	81.4(1)	81.4(1)
O1–M1–O1 ×2	91.7(1)	90.8(1)	90.6(1)	90.6(1)	90.3(1)	90.1(1)	89.8(1)	89.6(1)	89.5(1)
O1–M1–O1	170.4(1)	169.7(1)	169.5(1)	169.4(1)	169.0(1)	168.9(1)	168.6(1)	168.2(1)	168.1(1)
O1–M1–O2 ×2	89.0(1)	88.6(1)	88.5(1)	88.5(1)	88.1(1)	87.8(1)	87.3(1)	86.7(1)	86.5(1)
O1–M1–O2 ×2	89.7(1)	90.2(1)	90.3(1)	90.3(1)	90.3(1)	90.4(1)	90.4(1)	90.4(1)	90.6(1)
O1–M1–O2 ×2	97.1(1)	98.1(1)	98.4(1)	98.4(1)	99.1(1)	99.5(1)	100.2(1)	101.0(1)	101.3(1)
O1–M1–O2 ×2	170.5(1)	170.9(1)	171.1(1)	171.0(1)	170.9(1)	170.7(1)	170.4(1)	170.0(1)	169.8(1)
O2–M1–O2	99.6(1)	98.9(1)	98.6(1)	98.7(1)	98.8(1)	98.9(1)	99.2(1)	99.4(1)	99.4(1)
OAV [°]	48.2(5)	49.2(5)	49.6(5)	50.0(5)	53.3(5)	55.5(5)	59.6(5)	65.0(5)	67.3(5)
Si–O2	1.598(2)	1.595(1)	1.598(1)	1.597(1)	1.593(2)	1.593(2)	1.597(2)	1.596(2)	1.594(2)
Si–O3	1.629(2)	1.630(1)	1.629(1)	1.629(1)	1.630(2)	1.630(2)	1.630(2)	1.629(2)	1.632(2)
Si–O3	1.631(2)	1.631(1)	1.633(1)	1.634(1)	1.632(2)	1.634(2)	1.633(2)	1.637(2)	1.636(2)
Si–O1	1.636(2)	1.638(1)	1.637(1)	1.637(1)	1.638(2)	1.639(2)	1.639(2)	1.643(2)	1.642(2)
$\langle Si-O\rangle$	*1.624*	*1.624*	*1.624*	*1.624*	*1.623*	*1.624*	*1.625*	*1.626*	*1.626*
BLD [%]	0.8(1)	0.9(1)	0.8(1)	0.8(1)	0.9(1)	0.9(1)	0.9(1)	0.9(1)	1.0(1)
O1c1–Si–O3c1	108.8(1)	108.8(1)	108.7(1)	108.6(1)	108.3(1)	108.2(1)	107.9(1)	107.5(1)	107.3(1)
O1c1–Si–O3c2	107.4(1)	106.9(1)	106.7(1)	106.6(1)	106.6(1)	106.6(1)	106.5(1)	106.4(1)	106.5(1)
O1c1–Si–O2c1	115.1(1)	115.4(1)	115.5(1)	115.5(1)	115.4(1)	115.3(1)	115.1(1)	114.9(1)	114.7(1)
O2c1–Si–O3c1	110.2(1)	109.6(1)	109.6(1)	109.6(1)	109.6(1)	109.7(1)	109.7(1)	109.9(1)	109.9(1)
O2c1–Si–O3c2	105.5(1)	105.8(1)	105.9(1)	105.9(1)	106.2(1)	106.1(1)	106.4(1)	106.4(1)	106.6(1)
O3c1–Si–O3c2	109.9(1)	110.4(1)	110.5(1)	110.5(1)	110.8(1)	110.9(1)	111.3(1)	111.7(1)	111.9(1)
TAV [°]^2	10.7(5)	11.4(5)	11.7(5)	11.8(5)	11.5(5)	11.4(5)	11.0(5)	11.5(5)	11.1(5)
τ	110.4(1)	110.4(1)	110.3(1)	110.3(1)	110.1(1)	110.1(1)	109.3(1)	109.6(1)	109.5(1)
O3–O3–O3	177.6(1)	176.0(1)	175.9(1)	175.9(1)	173.3(1)	172.6(1)	170.3(1)	168.5(1)	167.4(1)

OAV $= \sum_{i=1}^{12} (\Theta_i - 90°)^2/11$ with Θ_i = O–M–O bonding angle (Renner and Lehmann, 1986);

TAV $= \sum_{i=1}^{6} (\Theta_i - 109.57°)^2/5$ with Θ_i = O–T–O bonding angle (Renner and Lehmann, 1986).

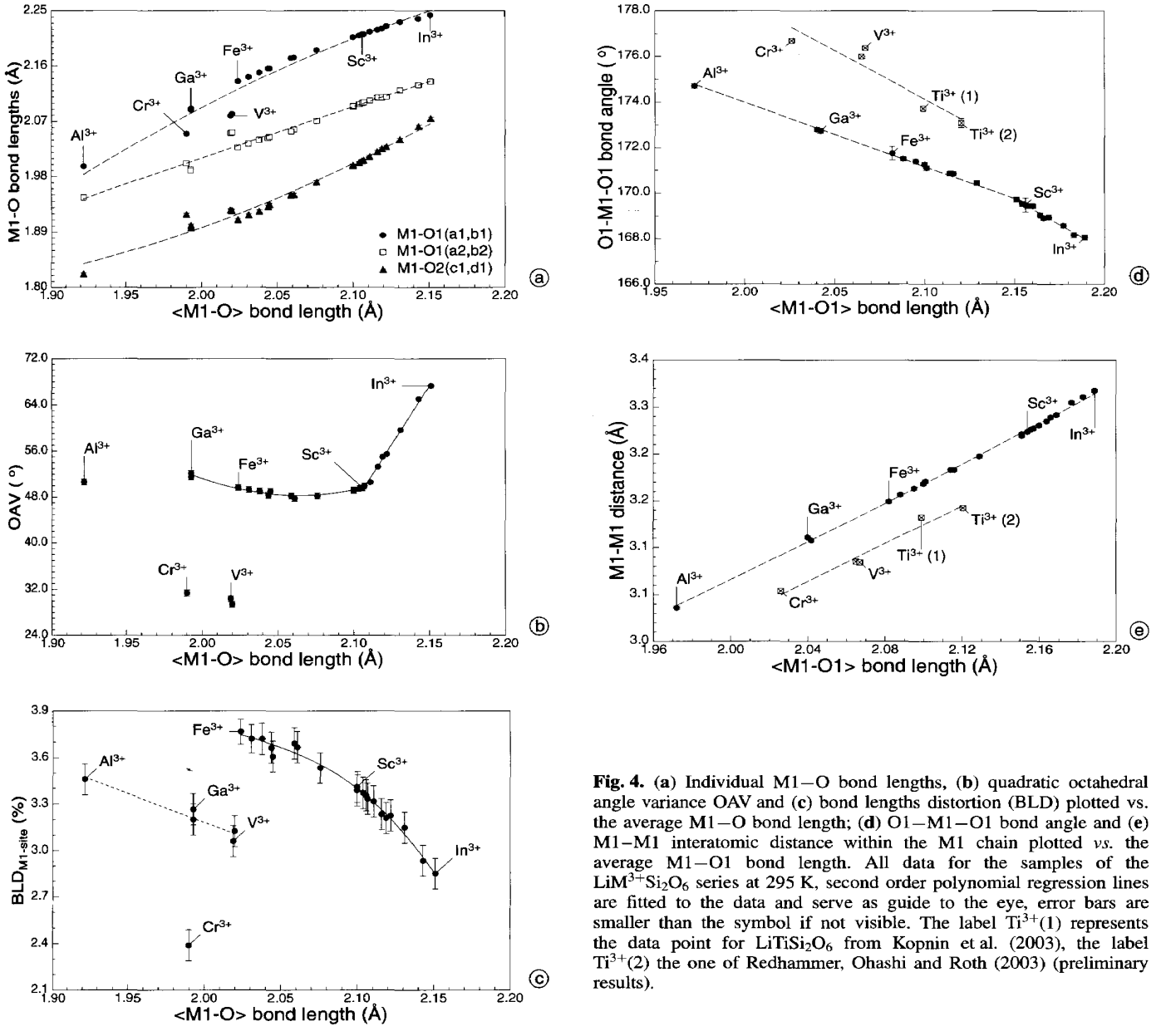

Fig. 4. (**a**) Individual M1—O bond lengths, (**b**) quadratic octahedral angle variance OAV and (**c**) bond lengths distortion (BLD) plotted vs. the average M1—O bond length; (**d**) O1—M1—O1 bond angle and (**e**) M1—M1 interatomic distance within the M1 chain plotted *vs.* the average M1—O1 bond length. All data for the samples of the $LiM^{3+}Si_2O_6$ series at 295 K, second order polynomial regression lines are fitted to the data and serve as guide to the eye, error bars are smaller than the symbol if not visible. The label $Ti^{3+}(1)$ represents the data point for $LiTiSi_2O_6$ from Kopnin et al. (2003), the label $Ti^{3+}(2)$ the one of Redhammer, Ohashi and Roth (2003) (preliminary results).

M1—O1 bond lengths. The latter two bonds are the ones, pointing form the M1 cation to the two O1 oxygen atoms, forming the common edge between two neighbouring octahedra. As can be seen from Figure 4e the data points for compounds having spherical M1 cations [Al^{3+}, Ga^{3+} ($3d^0$), Fe^{3+} ($3d^5$), Sc^{3+} ($3d^{10}$), In^{3+}] form a common, almost linear trend. The data for Cr^{3+} ($3d^3$), V^{3+} ($3d^2$) and Ti^{3+} ($3d^1$; preliminary results), with a non-spherical electron configuration distinctly fall of this trend. This shows that besides pure geometric considerations electronic effects also play an important role in defining the distortional state of the M1 octahedron.

If the M1 site is occupied by a small cation (e.g. Al^{3+}), the octahedral chain appears to be "shorter" than the tetrahedral one. In $LiAlSi_2O_6$, the M1—M1 distance is 3.043(2) Å only, in $LiCrSi_2O_6$ it is 3.065(2) Å. The cation-cation repulsion perpendicular to the O1(a2)—O1(b1) edge, which is common to two neighbouring octahedra, causes the two trivalent cations to move to the largest possible distance from each other and also out of the centres of the octahedra. The M1—O1(a1, b1) bond lengths in the equatorial plane become longer, the M1—O2(c1, d1) bond length shortens as compared to an octahedron with the cation in the centre of the anion-polyhedron. This displacement of the M1 cation has also been observed in the hedenbergite-aegirine $CaFe^{2+}Si_2O_6$—$NaFe^{3+}Si_2O_6$ solid solution series (Redhammer, 2001), where divalent iron is replaced by trivalent iron. The octahedra are stretched in chain direction, as can be seen from the rather large M1—O1(a2, b2) bond lengths. This enables the octahedral chain to fit to the tetrahedral chain. Li-clinopyroxenes having small cations on the M1 site show large M1—M1—M1 bond angles, e.g. 118.1(1)° in $LiAlSi_2O_6$, 114.7(1)° in $LiGaSi_2O_6$ as compared to 108.3(1)° in $LiInSi_2O_6$.

Increasing the size of the octahedral cation decreases the kinking of the tetrahedral chain, which shows a max-

imum elongation in c direction at 295 K in the compounds $LiGaSi_2O_6$ and $LiFeSi_2O_6$. Here the tetrahedral chains are fully expanded showing tetrahedral kinking-angles O3—O3—O3 very close to 180°. If the octahedra are expanded further by the substitution of even larger cations (Sc^{3+}, In^{3+}) into M1, the tetrahedral chain starts to hamper the expansion of the M1 chain in c direction. This explains the reduced increase of the M1—O1(a2, b2) bond lengths (Fig 4a) with increasing size of the octahedral cation. The O1(a2, b2) oxygen atom forms the common corner of the M1-octahedron and the SiO_4-tetrahedron and therefore constitutes the link between the two building units.

The substitution of larger cations on M1 is also reflected in the oxygen-oxygen interatomic distances. For most of the compounds, the average values for the unshared O—O distances (Fig. 5a) show a nearly linear correlation with the ionic radius of the octahedral cation. A similar behaviour is found for the average values of the shared O—O distances. However, the data for the $Li(Sc_{1-x}In_x)Si_2O_6$ series show a distinctly different slope for the average of the shared edges. The average of all O—O distances also reflects this different slope of the $Li(Sc_{1-x}In_x)Si_2O_6$ series. The variation of individual O—O interatomic distances is not uniform. The O1(a1)—O2(c1) distance (unshared edge, Fig. 5b), which runs along the b-axis within the equatorial plane of the octahedron, shows the largest change between $LiAlSi_2O_6$ and $LiInSi_2O_6$ and increases by 16.8%. Large changes of 13.1% and 11.8% take place for the O1(a1)—O1(c1) and the O2(c1)—O2(d1) edge. All of them are unshared edges. The smallest increase is observed for the O1(a1)—O1(a2) edge, which changes by only 4.2%. Within the $Li(Sc_{1-x}In_x)Si_2O_6$ series this distance stays constant. The oxygen atoms O1(a1) and O1(a2) form two corners of the octahedron and at the same time the apex of two corner sharing tetrahedra. Thus the O1(a1)—O1(a2) octahedral edge is hampered in its expansion due to the connection with the tetrahedral chain.

The O1(a1)—O1(b1) and the O1(a2)—O2(d1) octahedral edges (shared edges), which are common to the M1 site and the M2 polyhedron (Fig. 5c) also show small geometrical expansions of 6.6 and 6.9% within the series from the Al^{3+} and the In^{3+} compound. Within the $LiSc_{1-x}In_xSi_2O_6$ series these edge lengths stay nearly constant. The O1(a2)—O1(b1) edge, which is common to two octahedra, increases with the size of the M1 cation, however the expansion of this octahedral edge is also reduced within the $LiSc_{1-x}In_xSi_2O_6$ series. Similar to the small increase of the O1(a1)—O1(a2) edge lengths (Fig. 5b) this reduced increase is presumably related to the hampering influence of the tetrahedral chain. For $LiInSi_2O_6$ the three different shared octahedral edge lengths are similar. This is not the case for the Al^{3+} compound which has a significantly shorter O1(a2)—O1(b1) edge.

In general, the shared edges expand less than the unshared edges when larger cations are substituted to the M1 site. The ratio between unshared and shared edges e_u/e_s

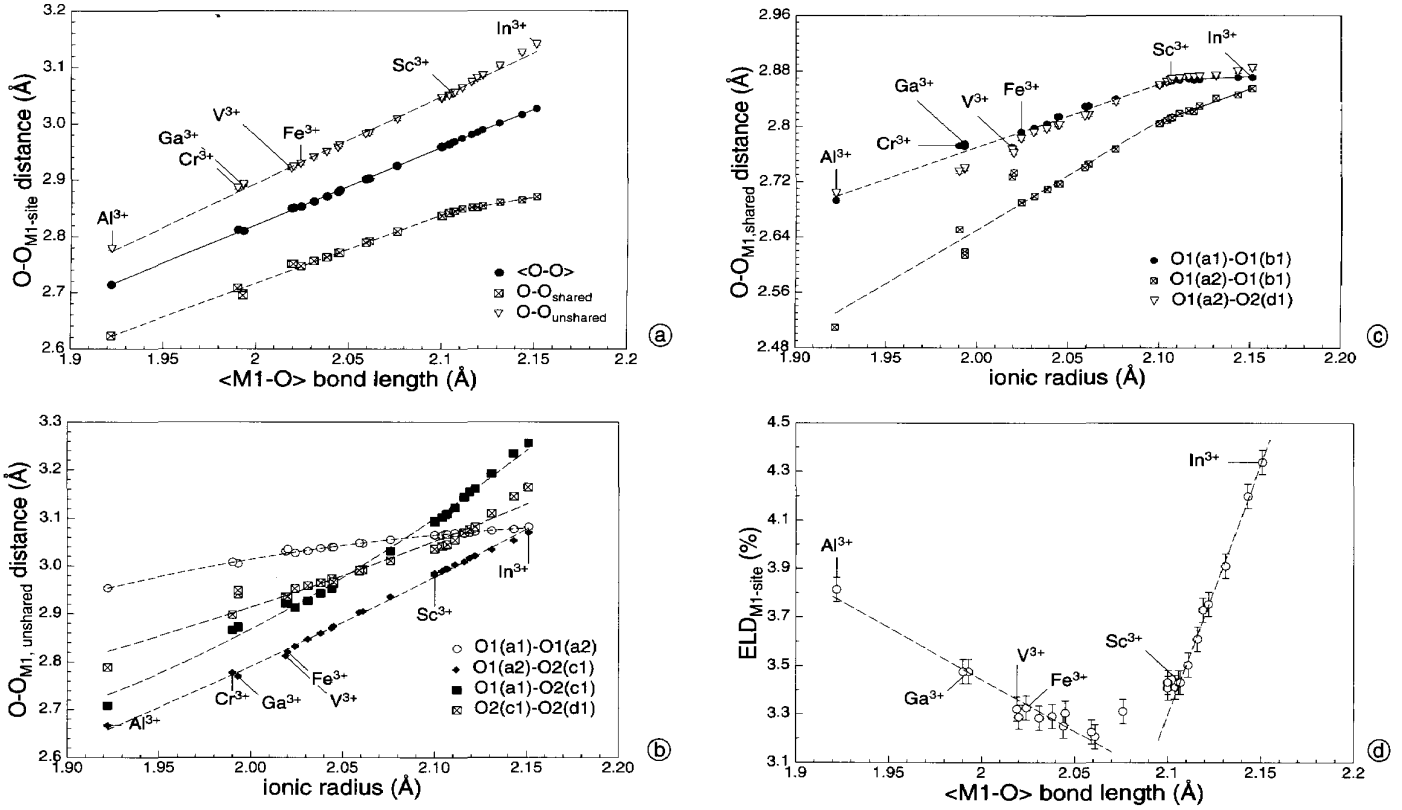

Fig. 5. Oxygen atom interatomic distances (O—O) defining edges of the M1-octahedron for the $LiMe^{3+}Si_2O_6$ series at 295 K. Error bars are smaller than the symbols if not visible; regression lines are fitted to the data as a guide to the eye. (**a**) average values for the M1 O—O distances, (**b**) individual values for the unshared O—O edges, (**c**) individual values for the shared O—O edge (**d**) edge lengths distortion (ELD).

increases linearly up to $LiScSi_2O_6$, for the $LiSc_{1-x}In_xSi_2O_6$ series, e_u/e_s again increases linearly however with different slope. The edge length distortion parameter (ELD[3], Fig. 5d) shows, similar to the octahedral angle variance, a slight decrease with increasing octahedral cationic radius r up to $r \approx 0.68$ Å (intermediate radius within the $LiFe_{1-x}Sc_xSi_2O_6$ series). A further increase of the ionic radius drastically increases the edge length distortion (Fig. 5d) and the octahedral angle variance (Fig. 4b).

This is predominately caused by the non uniform variation of the unshared octahedral edges. Among all Li-clinopyroxenes investigated in this study, the octahedron in $LiInSi_2O_6$ shows the largest deviation from an ideal octahedron, the most regular ones are found in $LiVSi_2O_6$ (Table 4).

The M2 polyhedron

Among all clinopyroxenes, the Li-clinopyroxenes $LiMe^{3+}Si_2O_6$ show the largest M2-site distortion. As has been discussed by Redhammer and Roth (2002), Li^+ prefers a 6-fold coordination in these compounds. This is mainly maintained by a displacement of the tetrahedral chain in c-direction relative to the octahedral chain. As a consequence, the Li-clinopyroxenes show large monoclinic angles of about 110°, whereas in Na^+ clinopyroxenes they are close to about 107° and in Ca^{2+}-clinopyroxenes they amount to ≈105°. In the two latter groups of compounds, the M2 site is 8-fold coordinated. As a consequence of the displacement of the tetrahedral chains, two of the four shorter M2—O3 distances move out of the coordination sphere of the M2 cation, the M2 site becomes 6-fold coordinated (Redhammer and Roth, 2002). Within the Li-clinopyroxene series, the M2—O bond lengths show distinct variations with the size of the octahedral M1 cation. In $LiAlSi_2O_6$ the M2—O2 and M2—O3 bond lengths are of similar size, the M2—O1 bond length is the shortest one. All six bonds, however, lie within 2.100(2) and 2.282(2) Å.

In contrast to the average M2—O bond (Fig. 6a), the behaviour of the individual M2—O bond lengths (Fig. 6b) is more complex: With increasing size of the M1 cation (increasing average M1—O bond length), the M2—O2 bond lengths decrease, the M2—O1 is fairly constant and the M2—O3 bond lengths steadily increase. As outlined above, the repulsion forces between the highly charged M1 cations cause a stretching of the M1—O1(a1, b1) bond and a shortening of the M1—O2(c1, d1) bond. Because of this, the M2—O1(a1, b1) bond length is distinctly shorter than the M2—O2(c1, d1) in $LiAlSi_2O_6$. With increasing size of the M1 cation, the M2—O2 distance decreases over the whole $LiMe^{3+}Si_2O_6$ series. Data for the $LiFe_{1-x}Sc_xSi_2O_6$ and the $LiSc_{1-x}In_xSi_2O_6$ series exhibit different slopes. The M2—O1 bond length decreases only slightly between the Al^{3+} and the Fe^{3+} compound. In the $LiFe_{1-x}Sc_xSi_2O_6$ series it slightly increases so that in the Sc^{3+} end-member the M2—O1 and M2—O2 bond lengths are very similar. For the $LiSc_{1-x}In_xSi_2O_6$ series, M2—O1 again decreases but with a smaller slope than for the M2—O2 bond length. In the Li-clinopyroxenes with large M1 cations, the Li^+ cation is placed closer to the M1 chain than e.g. in the Al^{3+} compound. This is also reflected by the shift of the Li(y) fractional atomic coordinate, which moves from 0.2492(7) in $LiInSi_2O_6$ to 0.2746(5) in $LiAlSi_2O_6$. The increase of the M2—O3 bond length is directly linked to the kinking of the tetrahedral chain. The M2—O3 distance and the O3—O3—O3 angle within the tetrahedral chain show a strong negative correlation (not shown).

Throughout the whole $LiMe^{3+}Si_2O_6$ series the Li^+-polyhedra are isolated and do not share a common edge with other Li^+ sites (due to the loss of two additional Li—O3 bonds). This is different to the Ca^{2+} or Na^+ clinopyroxenes where the M2 site is 8-fold coordinated and forms-like the M1 sites-a zig-zag chain along the c-axis. In $LiInSi_2O_6$ four Li—O bond lengths are within 2.018(2) and 2.080(2), the two others are 2.828(2) Å, thus the oxygen coordination of Li^+ is better described as a 4-fold rather than a 6-fold one in the Li-clinopyroxenes with large M1 cations. This is in accordance with recent findings of Downs (2003) who stated that Li^+ is 4-fold coordinated in some clinopyroxenes such as $LiScSi_2O_6$, but 6-fold coordinated in others, such as $LiAlSi_2O_6$.

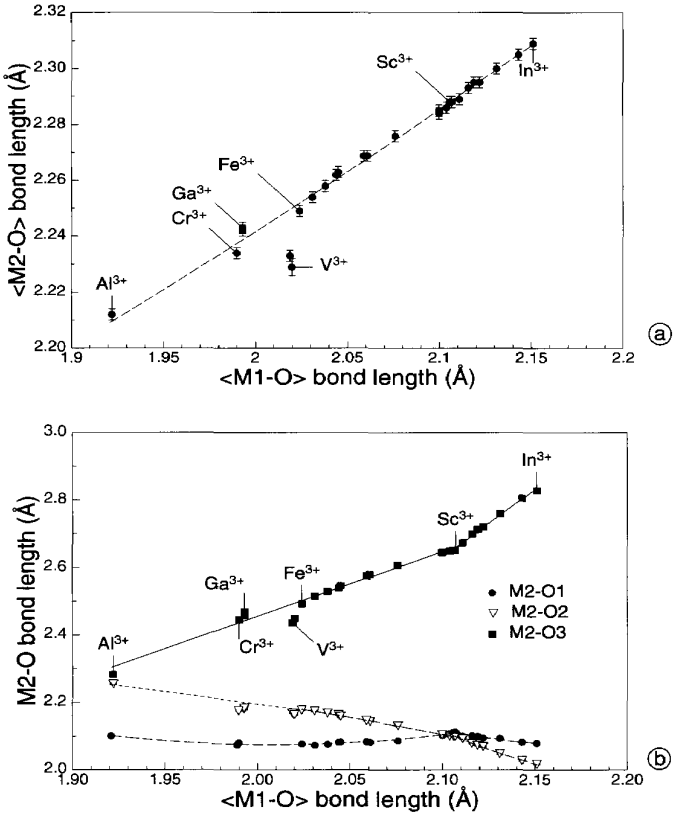

Fig. 6. Average (**a**) and individual (**b**) M2—O bond lengths in the $LiMe^{3+}Si_2O_6$ series at 295 K as a function of the observed average M1—O distance. Regression lines (linear for small, quadratic for larger radii) have been fitted to the data and serve as a guide to the eye, error bars are smaller than the symbols if not visible.

[3] $\mathrm{ELD} = \frac{100}{n}\sum_{i=1}^{n}\frac{|(O-O)_i - (\langle O-O\rangle)|}{(\langle O-O\rangle)}$ %, n = amount of edges and (O—O) = oxygen-oxygen interatomic distance defining an edge of the octahedron.

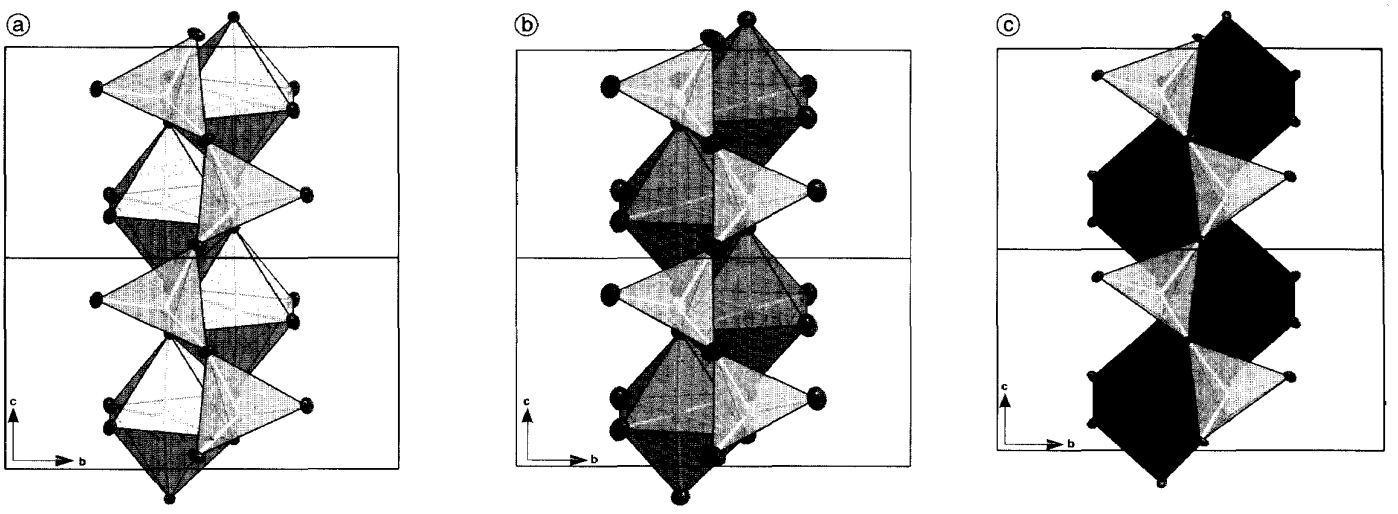

Fig. 7. Section of the structure of (**a**) $LiAlSi_2O_6$ having S-rotated tetrahedral chains with O3—O3—O3 = 189.8(1)° (**b**) $LiCrSi_2O_6$ having nearly fully extended tetrahedral chains with O3—O3—O3 = 179.0(1)° and (**c**) $LiInSi_2O_6$ having O-rotated chains with O3—O3—O3 = 167.4(1)°.

The tetrahedral site

Thompson (1970) has described two different rotational senses of the tetrahedral chain relative to the octahedral one, the S-(same) and the O-(opposite)-rotation. In an S-rotation the triangular face of the tetrahedron and the one of the octahedron have the same orientation within the *b-c* plane when the tetrahedral chain is rotated to an extreme angle of 120°. In the O-rotation they have different orientations (Figure 7). Most clinopyroxenes show an O-rotation. One exception is spodumene $LiAlSi_2O_6$ (S-rotation) which has the largest bridging angle of 189.8(1)°. Changes in the size of the octahedral chain have to be accommodated by the tetrahedral chain also: One mechanism is the reduction of the kinking of the tetrahedral bridging angle O3—O3—O3.

Starting from $LiAlSi_2O_6$ (Fig. 7a) an increase of the size of the octahedral M1-cation can be accommodated by a stretching of the tetrahedral chain (Fig. 8). In the Ga^{3+}, Cr^{3+} (*C2/c* HT-phase) V^{3+} and Fe^{3+} compounds, this mechanism is active and the tetrahedral chains are nearly fully extended.

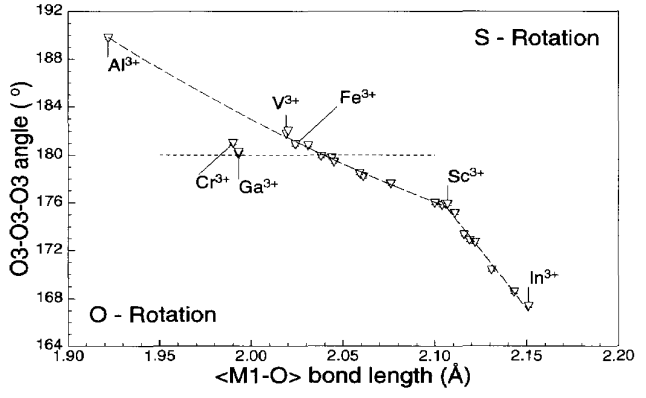

Fig. 8. Changes of the O3—O3—O3 tetrahedral kinking angle with increasing size of the octahedral M1 cation. A short-dashed horizontal line marks 180°, where the chains are fully extended and the change from S- to O-rotation takes place. Error bars are smaller than the symbols.

For the larger M1-cations, i.e. for the $LiFe_{1-x}Sc_xSi_2O_6$ series, $LiScSi_2O_6$ and $LiInSi_2O_6$ the geometrical difference between octahedral and tetrahedral chain cannot be reduced by a stretching of the tetrahedral chain alone. Different mechanisms have to become active: The chains get kinked again (Fig. 8). This behaviour goes along with the decreasing M1—M1—M1 angle, which is a result of the increasing size of the octahedra and the decreasing repulsion forces between M1 cations. The M1—M1—M1 angle amounts to 112.7(1)° in $LiFeSi_2O_6$ and to 108.3(1)° in $LiInSi_2O_6$.

Additionally to the chain kinking, alterations in the Si—O bond lengths and the O—O tetrahedral edge lengths are necessary. The average Si—O bond length (Fig. 9a) slightly increases from the Al^{3+} to the In^{3+} compound. However not all individual Si—O bonds (Fig. 9b) are positively correlated with the size of the octahedral cation and no uniform variation across the $LiMe^{3+}Si_2O_6$ series is present. The two Si—O3 bonds (which are the two bridging Si—O bonds, $Si—O_{br}$), remain constant within experimental error from Me = Al^{3+} to Fe^{3+}. The Ga^{3+} to Fe^{3+} compounds are those with nearly fully extended tetrahedral chains. As no further expansion of the tetrahedral chain by decreasing the tetrahedral kinking is possible when substituting larger cations than Fe^{3+}, the bond lengths are stretched in [001] direction. This behaviour is clearly visible, when plotting $Si—O_{br}$ distances *vs.* ⟨M1—O⟩ (Fig. 9c). The Si—O1 bond, which points along *a*, remains constant between the V^{3+} and the Sc^{3+} compound but increases within the Sc^{3+}—In^{3+} series, whereas the Si—O2 bond length-pointing in *b* direction, decreases from V^{3+} to In^{3+}. The latter decrease of Si—O2 suggests that the expansion of the octahedral chain in *b*-direction compresses the tetrahedron in *b* direction (Fig. 9a). On the average, the $Si—O_{nbr}$ distance (average of Si—O1 and Si—O2) remains quite constant over the complete series. Small decreases (Fe—Sc series) and increases (Sc—In series) might be inferred from the data in Figure 9c, however, these changes are within two estimated standard deviations.

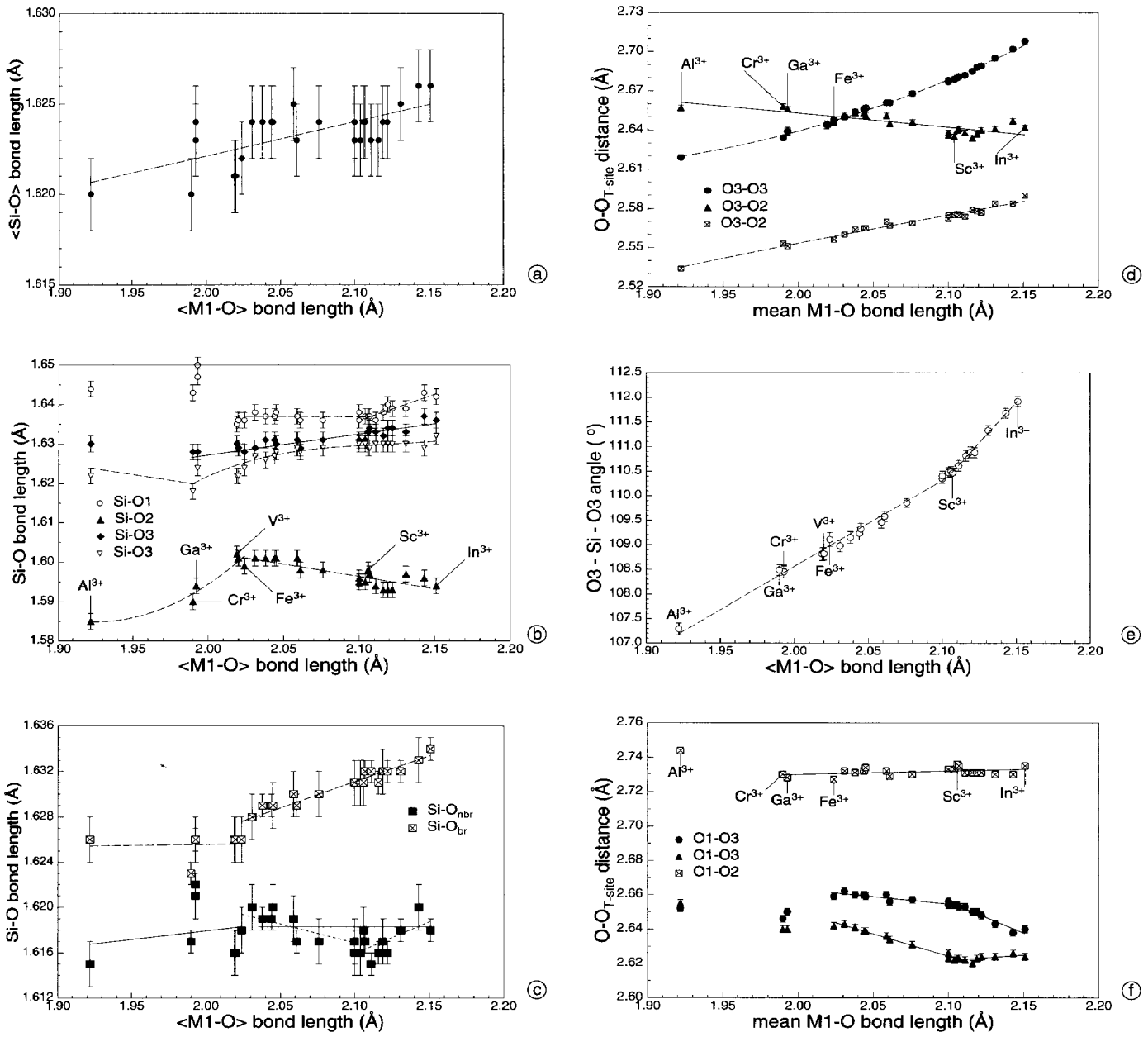

Fig. 9. Structural variations within the tetrahedral site for the $LiMe^{3+}Si_2O_6$ series at 295 K (**a**) average Si—O bond lengths (**b**) individual Si—O bond lengths (**c**) bridging ($Si-O_{br}$) and non-bridging ($Si-O_{nbr}$) Si—O distances (**d**) O—O oxygen atom distances defining the edges of the basal triangular face of the tetrahedron (**e**) O3—Si—O3 bond angle and (**f**) distances of oxygen atoms of the basal plane to the O1 apex oxygen atom.

The most pronounced changes within the tetrahedron are reflected by the O—O distances. The triangular face spanned by the O2 and O3 oxygen atoms changes most strongly (Fig. 9d). The O3—O3 distance increases by 3.5% from the Al^{3+} to In^{3+} compound, accompanied by a steady increase of the O3—Si—O3 bond angle from 107.3(1)° to 111.9(1)° (Fig. 9e). This alteration allows an elongation of the tetrahedron along *c* without a marked change of the Si—O bond lengths (Fig. 9b). An increase in lengths by 2.2% is also observed for one of the two O2—O3 edges, whereas the other one decreases. The changes in O2—O3 edge lengths result from a rather large shift of the O2 oxygen atom in *c* direction within the $LiMe^{3+}Si_2O_6$ series. In $LiAlSi_2O_6$, the tetrahedron appears to be elongated along *a* and *b* (large O1—Si—O2 and O2—Si—O3 angles), whereas it is elongated along *b* and *c* in $LiInSi_2O_6$ (large O1—Si—O2 and O3—Si—O3 angles). The elongation in *c* is necessary to fit octahedral and tetrahedral chains.

The O—O oxygen atom distances from the basal O2 and O3 atoms of the triangular face to the O1 apex oxygen atom remains constant (O1—O2 distance) or decrease (O1—O3 distances, Fig. 9f) with increasing ⟨M1—O⟩. The decrease of these $O_{basal}-O_{apex}$ distances, which is non-uniform throughout the $LiMe^{3+}Si_2O_6$ series, correlates with the decrease of the two O1—Si—O3 and the O1—Si—O2 bond angles. The average of these angles, named the angle τ, decreases with increasing size of the octahedral cation (Fig. 10).

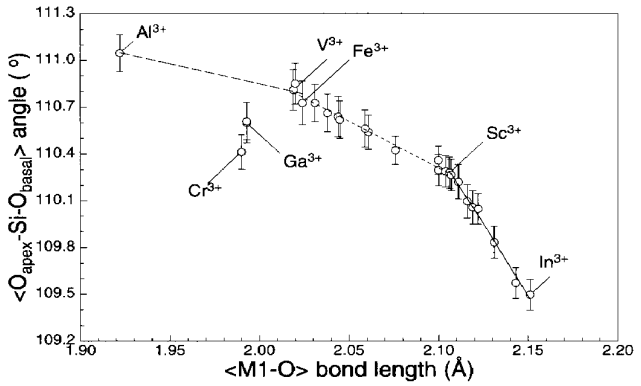

Fig. 10. Average of the O1–Si–O2 and O1–Si–O3 bond angles (angle τ) for the $LiMe^{3+}Si_2O_6$ series at 295 K.

The decrease of τ, which is a result of the elongation of the tetrahedron along c, reduces the length of the tetrahedral chain in a direction. For the $LiSc_{1-x}In_xSi_2O_6$ series, the distinct decrease of τ obviously compensates the increase of the octahedral chain length induced by the substitution of the smaller Sc^{3+} by In^{3+}. Thus the a lattice parameter of $LiSc_{1-x}In_xSi_2O_6$ stays constant within this solid solution series. The different nature of the $LiSc_{1-x}In_xSi_2O_6$ series is also reflected in the variation of the Si–O–Si bond angle (Fig. 11). Up to $LiScSi_2O_6$, the size of the M1 cation is positively correlated with the Si–O–Si angle. This reflects the stretching of the tetrahedral chain along c as a consequence of the increasing M1 cation. In $LiScSi_2O_6$ the Si–O–Si angle amounts 143.3(1)°. We note that a further increase of the Si–O–Si angle within the $LiSc_{1-x}In_xSi_2O_6$ does not take place and thus seems to be (energetically) impossible. Included in Figure 11 are Si–O3–Si vs. ⟨M1–O⟩ data for the Ca- and Na-clinopyroxene series. From this it is evident that the highest Si–O3–Si bond angle, observed in the *C2/c* clinopyroxenes is 143.5(1)° and it is found for $LiSc_{0.74}In_{0.26}Si_2O_6$. Obviously, this is a limiting value for the Si–O3–Si bond angle in the C2/c clinopyroxenes. As

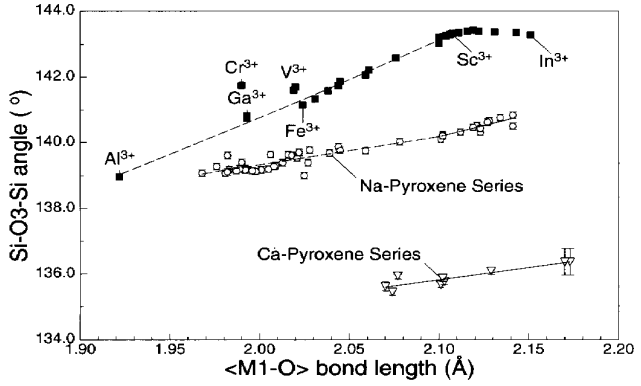

Fig. 11. Si–O3–Si bond angle for the $LiMe^{3+}Si_2O_6$ series at 295 K. Data for the $NaMe^{3+}Si_2O_6$ series are from Clark et al. (1969); Hawthorn and Grundy (1973, 1974); Ohashi, Osawa, Tsukimura (1987); Ohashi, Osawa, Sato (1990, 1994a, 1994b); Ohashi (2003) and Redhammer et al. (2003); data for the $CaMe^{2+}Si_2O_6$ series from Redhammer (2001), Ghose, Wan and Okamura (1987) and Freed and Peacor (1967).

the tetrahedral chain cannot be stretched by an increase of the Si–O3–Si bond angle within the $LiSc_{1-x}In_xSi_2O_6$ series, a larger flattening of the tetrahedra itself (decreasing O_{basal}–Si–O_{apex} bond angle, Fig. 10) takes place. This explains the different slope of the angel τ *vs.* ⟨M1–O⟩ data for the Sc-In series, being equal to a smaller elongation of the tetrahedron along [100] and a larger stretching along [001].

Bond-lengths-bond-strengths calculations have shown that throughout the complete Li-clinopyroxene series, silicon and the M1 cation are saturated (bond valence sums $\Sigma s = 3.99 - 4.02$ and $\Sigma s = 3.00 - 3.03$ respectively). The Li-cation generally is under-bonded and possesses valence sums of $\Sigma s = 0.79 - 0.82$. There is no systematic variation of valence sums throughout the $LiMe^{3+}Si_2O_6$ series for lithium. It is assumed that the long distant Li–O3 bonds are responsible for the low valence sum. The O1 oxygen atom also is saturated in charge, except $LiAlSi_2O_6$ (under-bonded with $\Sigma s = 1.95$) and $LiInSi_2O_6$ (over-bonded with $\Sigma s = 2.07$). The O2 oxygen atom, however, possesses a distinct deficit in negative charge (under-bonded). Thereby this deficit decreases from $LiAlSi_2O_6$ ($\Sigma s = 1.80$) to $LiInSi_2O_6$ ($\Sigma s = 1.94$). The apparent deficit in negative charge is compensated for by the short Si–O2 and M2–O2 bond lengths. The large O1–Si–O2 bond angle may also result from this greater repulsion between the non-bridging oxygen atoms. Contrarily to this, the O3 oxygen atom shows distinct over-bonding in the Al^{3+} compound ($\Sigma s = 2.11$). This surplus in negative charge decreases with increasing size of the M1 cation. In the Sc^{3+} compound O3 is balanced in charge, in the In^{3+} one it is under-bonded ($\Sigma s = 1.95$).The surplus in charge is compensated for by rather long Si–O3 bond lengths and large Li–O3 bonds. Kimata, Saito, Matsui, Shimizu and Nishida (1998) argued that large atomic displacements may arise from either over-bonding or under-bonding. Over-bonding supposedly directs repulsive energy to the nearest neighbour atoms (oxygen atoms), resulting in dynamical positional disorder. This correlation, noted by the above authors and by Redhammer and Roth (2003) for thortveitite compounds, also holds true for the Li-clinopyroxene series.

Conclusions

- Within the $LiMe^{3+}Si_2O_6$ series, cations ranging from 0.53 Å (Al^{3+}) to 0.79 Å (In^{3+}) can be substituted on the M1 site. The attempt to substitute even larger cations such as Y^{3+} was not successful in this study as the geometrical difference of the octahedral M1 chain and the SiO_4 tetrahedral chain becomes too large.
- The compounds $LiVSi_2O_6$ and $LiCrSi_2O_6$ (in the high temperature *C2/c* phase) deviate from the trends observed for the other structural parameters. This is due to the different electronic nature of the M1 site cations Cr^{3+} and V^{3+} with an aspheric electronic configuration ($3d^3$ and $3d^2$ configuration, respectively).
- Increasing the size of the M1 cation results in structural changes in all three building units of the structure, $M1O_6$-octahedron, SiO_4 tetrahedron and Li-polyhedron.

- With increasing ionic size of the M1 cation, the octahedra become tetragonal compressed along the *c*-direction, the M1 cation is displaced from the centre of the octahedron due to cation-cation repulsion forces perpendicular to the O1–O1 octahedral edge as is the case for smaller M1-cations.
- There are non-uniform increases of bond- and edge lengths as well as bond angles which are the result of the structural adjustments required to maintain a good fit between octahedral and tetrahedral chain. Remarkable is the overall small increase (4.2%) of the octahedral edge built up by the O1(a1) and O1(a2) oxygen atoms, which, at the same time, are two apex oxygen atoms of two corner sharing SiO_4 tetrahedra. This has to be compared to the O1(a1)–O2(c1) edge running along *b* in the equatorial plane of the octahedron, that increases by 16.8% within the same compositional range.
- The tetrahedral chain exhibits a S-rotational sense in $LiAl^{3+}Si_2O_6$ with a tetrahedral kink angle O3–O3–O3 of 189.8(1)°. For small M1 cations, the linkage between tetrahedral and octahedral chain can be maintained by stretching the SiO_4 chain (decreasing the O3–O3–O3 angle to 180°) along *c*. Compounds with Ga^{3+}, V^{3+} and Fe^{3+} have nearly fully expanded chains (O3–O3–O3 ≈ 180°).
- A further increase of the M1 ionic size cannot be maintained by a sole stretching of the tetrahedral chains. Substituting cations larger than Fe^{3+} again causes a kinking of the tetrahedral chain, however, with a different rotational sense (O-rotation). Additionally, distinct edge length as well as bond angle alterations within the SiO_4 tetrahedron are also observed. It is the O3–O3 tetrahedral edge and the Si–O3–Si bond angle, which are altered to stretch the chain along [001].
- Within the Sc-In series, a maximum Si–O3–Si bond angle of 143.5(1)° is reached which represents the highest value observed within the (*C*2/*c*) clinopyroxenes and which obviously represents an upper limit for this angle. Instead of changing the Si–O3–Si bond angle within the Sc-In series, the angle τ is decreases more distinctly as compared to the e.g. Fe-Sc series to match octahedral and tetrahedral chains. Thus the tetrahedron, which is elongated along *a* and *b* in $LiAlSi_2O_6$, becomes elongated along *c* with increasing size of the M1 cation. The elongation along *a* decreases. This mechanism seems to be most effective for very large M1-cations.

Acknowledgments. GJR would like to thank the Austrian Academy of Science for the financial support through and APART (Austrian Program for Advanced Research and Technology) scholarship in 2000–2003. We are grateful to Volker Kaiser for his help in the X-ray diffraction laboratory and Josef Ernst for his kind support with the high pressure synthesis experiments. We further thank for the constructive and very detailed reviews of Eugen Libowitzky (Vienna) and an anonymous referee which helped to increase the impact of the paper.

References

Behruzi, M.; Banerjea-Appel, E.; Hahn, Th.; Scherberich, F. D.: Flux growth of $LiFeSi_2O_6$, $LiCrSi_2O_6$ and $LiFeGe_2O_6$. Z. Kristallogr. **167** (1984a) 212–214.

Behruzi, M.; Hahn, Th.; Prewitt, C. T.; Baldwin, K.: Low- and high-temperature structures of $LiFeGe_2O_6$, $LiFeSi_2O_6$ and $LiCrSi_2O_6$. Acta Cryst. **A40** (1984b) Suppl. **C-247**.

Brown, W. L.: On lithium and sodium trivalent-metal pyroxenes and crystal field effects. Min. Mag. **38** (1971) 43–48.

Burnham, C. W.; Clark, J. R.; Papike, J. J., Prewitt, C. T.: A proposed crystallographic nomenclature for clinopyroxene structures. Z. Kristallogr. **125** (1969) 109–119.

Clark, J. R.; Appleman, D. E.; Papike, J. J.: Crystal-chemical characterisation of clinopyroxenes based on eight new structure refinements. Min. Soc. Amer. Spec. Papers **2** (1969) 31–50.

Drysdale, D. J.: Hydrothermal synthesis of various spodumenes. Am. Mineral. **60** (1975) 105–110.

Downs, R. T.: Topology of the pyroxenes as a function of temperature, pressure, and composition as determined from the procrystal electron density. Am. Mineral. **88** (2003) 556–566.

Freed, R. L.; Peacor, D. R.: Refinement of the crystal structure of johannsenite. Am. Mineral. **52** (1967) 709–720.

Ghose, S.; Wan, C.; Okamura, F. P.: Crystal structures of $CaNiSi_2O_6$ and $CaCoSi_2O_6$ and some crystal-chemical relations in *C*2/*c* clinopyroxenes. Am: Mineral. **72** (1987) 375–381.

Grotepaß, M.; Behruzi, M.; Hahn, T.: Strukturen, Polymorphie und Mischkristallbildung im System $LiScSi_2O_6$–$LiInSi_2O_6$–$LiScGe_2O_6$–$LiInGe_2O_6$. Z. Kristallogr. **162** (1983) 90–91.

Hawthorne, F. C.; Grundy, H. D.: Refinement of the crystal structure of $NaScSi_2O_6$. Acta Cryst. **B29** (1973) 2615–2616.

Hawthorne, F. C.; Grundy, H. D.: Refinement of the crystal structure of $NaInSi_2O_6$. Acta Cryst. **B30** (1974) 1882–1884.

Hawthorne, F. C.; Grundy, H. D.: Refinement of the crystal structure of $LiScSi_2O_6$ and structural variations in the alkali pyroxenes. Can. Mineral. **15** (1977) 50–58.

Ito, J.; Frondel, C.: Syntheses of the scandium analogues of aegirine, spodumene, andradite and melanotektite. Am. Mineral. **53** (1968) 1276–1280.

Kimata, K.; Saito, S.; Matsui, T.; Shimizu, M.; Nishida, N.: Geochemical understanding as to the crystal structure of thortveitite: The ultimate in REE fractionation and the end of magmatism. N. Jb. Miner. Mh. **1998** (1998) 361–372.

Kopnin, E. M.; Sato, A.; Takayama-Muromachi, E.: High pressure synthesis and structure refinement of $LiTiSi_2O_6$. J. Alloys Compounds **354** (2003) L16–L19.

Ohashi, H.; Osawa, T.; Tsukimura, K.: Refinement of the structure of manganese sodium dimetasilicate. Acta Cryst. **C43** (1987) 605–607.

Ohashi, H.; Osawa, T.; Sato, A.: Structures of $Na(In,Sc)Si_2O_6$ clinopyroxenes formed at 6 GPa pressure. Acta Cryst. **B46** (1990) 742–747.

Ohashi, H.; Osawa, T.; Sato, A.: $NaScSi_2O_6$. Acta Cryst. **C50** (1994a) 838–840.

Ohashi, H.; Osawa, T.; Sato, A.: $NaVSi_2O_6$. Acta Cryst. **C50** (1994b) 1652–1655.

Ohashi, H.: X-ray Study on Si–O Bonding (2003). 295 pages, Maruzen Publishing Service, Tokyo, ISBN4-89630-094-7.

Redhammer, G. J.: Kontrollierte chemische Substitutionen in ausgewählten Ketten und Schichtsilikaten: Beiträge von Mössbauerspektroskopie und Einkristall-Röntgenbeugung zur Kristallchemie von Glimmern und Pyroxenen. Habilitation Thesis (2001) RWTH – Aachen, 335 pp.

Redhammer, G. J.; Roth, G.; Paulus, W.; Andre, G.; Lottermoser, W.; Amthauer, G.; Treutmann, W.; Koppelhuber-Bitschnau, B.: The crystal and magnetic structure of Li-Aegirine $LiFe^{3+}Si_2O_6$: a temperature dependent study. Phys. Chem. Minerals **28** (2001) 337–346.

Redhammer, G. J.; Roth, G.: Structural variations in the aegirine solid-solution series $(Na,Li)FeSi_2O_6$ at 298 K and 80 K. Z. Kristallogr. **217** (2002) 63–72.

Redhammer, G. J.; Roth, G. J.: β-$Y_2Si_2O_6$, a new thortveitite-type compound, determined at 100 and 280 K. Acta Cryst. **C59** (2003) i103–i106.

Redhammer, G. J.; Ohashi, H.; Roth, G.: Single-crystal structure refinement of $NaTiSi_2O_6$ clinopyroxene at low temperatures ($298 < T < 100$ K). Acta Cryst. **B59** (2003) 730–746.

Redhammer, G. J.; Roth, G.: The temperature dependent $C2/c \rightarrow P2_1/c$ phase transition in $LiMe^{3+}Si_2O_6$ clinopyroxenes with Me^{3+} = Ga, Cr, V, Fe, Sc and In. Z. Kristallogr. In press.

Renner, B.; Lehmann, G.: Correlation of angular and bond lengths distortion in TO_4 units in crystals. Z. Kristallogr. **175** (1986) 43–59.

Rodrigues-Carvajal, J.: Recent developments of the program FULLPROF. CPD Newsletter **26** (2001) 12–19; http://www.iucr.org/iucr-top/comm/cpd/Newsletters/

Sato, A.; Osawa, T.; Ohashi, H.: $LiGaSi_2O_6$. Acta Cryst. **C50** (1994) 487–488.

Satto, C.; Millet, P.; Galy, J.: Lithium Vanadium Metasilicate, $LiVSi_2O_6$. Acta Cryst. **C53** (1997) 1727–1728.

Shannon, R. D.; Prewitt, C. T.: Effective ionic radii in oxides and fluorides. Acta Cryst. **B25** (1969) 925–934.

Sheldrick, G. (1997) SHELXL, a program for refining crystal structures. University of Göttingen, Germany.

Stoe & Cie: X-SHAPE and X-RED: programs for optimising of the crystal shape (w.r.t. the merging R-value) and numerical absorption correction. Stoe & Cie (1996)

Thompson, Jr., J. B.: Geometric possibilities of amphibole structures and biopyroboles. Am. Mineral. **55** (1970) 292–293.

Toraya, H.: Distortions of octahedra and octahedral sheets in 1M micas and the relation to their stability. Z. Kristallogr. **157** (1981) 173–190.